Short-range atomic structure of $Nd_{2-x}Ce_xCuO_{4-y}$ determined by real-space refinement of neutron-powder-diffraction data

S. J. L. Billinge* and T. Egami

Department of Materials Science and Engineering and Laboratory for Research on the Structure of Matter, University of Pennsylvania, Philadelphia, Pennsylvania 19104-6272

The local structure of $Nd_{2-x}Ce_xCuO_{4-y}$, for $x = 0.165$ and 0.2, has been examined in detail. The technique used is the refinement of the atomic pair density function (PDF), which was obtained from neutron-powder-diffraction data. This is a nonstandard technique and thus it is described in some detail in this paper. We find that the CuO_2 planes in these materials are not flat but are buckled and distorted by oxygen displacements of magnitude $\lesssim 0.1$ Å. The displacements cannot be explained simply by the presence of different-sized impurity dopant ions in the lattice. The local structure is best explained if the CuO_2 planes are spatially inhomogeneous. There are two types of local regions, or domains, one heavily distorted and the other relatively undistorted. The structure within the distorted regions is well ordered with a distinct symmetry that is lower than that of the parent structure. A model for this local order is presented. From the PDF we estimate the size of these domains to be ~ 6 Å. Ion-size arguments suggest that the CuO_2 plane is in tension in this material and plane-buckling distortions are not expected from steric arguments. We present a mechanism whereby the buckling could be stabilized by a strong coupling to the electronic system via narrow-band O p states. This gives rise to lattice-induced hole states that coexist with the usual, impurity-doped, electrons. We speculate on the possible implications this has for the superconductivity of this material.

I. INTRODUCTION

It is becoming quite apparent that fine details of the atomic structure have a strong influence on the properties of high-T_c superconductors (HTSC). For example, it is known that the degree of oxygen vacancy ordering in reduced $YBa_2Cu_3O_{7-y}$ samples significantly affects T_c.[1] This was graphically illustrated by quenching and annealing experiments. T_c was suppressed by the quench but subsequently increased after a short room-temperature anneal.[2] This behavior could be correlated with an increase in the degree of oxygen vacancy ordering in the material.[3]

One of the most remarkable correspondences between small structural modifications and large scale changes in properties is exhibited in $La_{1.875}Ba_{0.125}CuO_4$ associated with the appearance of the low-temperature tetragonal (LTT) phase. The superconducting transition and Meissner fraction are dramatically suppressed and the oxygen isotope effect is enhanced,[4,5] yet the structural change associated with this transition is very subtle. This indicates a strong coupling of the lattice and the electronic system.

There are observations that the atomic structure is directly involved in the superconductivity. Anomalies have been seen associated with the appearance of superconductivity in various experiments which are sensitive to structure. These anomalies are too large to be explained by a strong coupling to regular phonons;[6,7] rather, they suggest the significance of local lattice distortions. Recently, Lang et al.[8] reported anomalies in thermal ex-

pansivity $[\alpha(T)]$ measurements of various superconductors. Although thermal expansivity is a long-range structure parameter, the origin of the anomalies in $\alpha(T)$ are best explained by insufficiently screened local structural distortions.[8] Experiments directly sensitive to local structure have shown strong evidence of structural instabilities associated with superconductivity. A change was seen in the copper extended x-ray-absorption fine-structure spectra in $YBa_2Cu_3O_7$ samples at T_c.[9] A distinct increase in the He ion channeling angle at T_c in $(Y,Er)Ba_2Cu_3O_{7-y}$ and $(Bi_{1.7}Pb_{0.3})Sr_2CaCu_2O_x$ samples[10] indicates that local atomic structure is becoming more ordered as the sample becomes superconducting. Our own pair density function (PDF) analyses of neutron-powder-diffraction data have indicated changes in the local structure associated with the appearance of superconductivity in a number of samples.[11-13] As will be discussed in this paper, the changes in the PDF can be explained as a modification of the local ordering arrangement of oxygen displacements.

There is evidence from PDF studies of $Tl_2Ba_2CaCu_2O_8$ that the observed local structure distortions are dynamic.[14] The PDF results presented in this paper are also best explained if the oxygen displacements are dynamic. It is thus interesting that an anomaly has recently been reported by Arai et al.[15] in the lattice dynamic spectrum of $YBa_2Cu_3O_{7-y}$, as observed by inelastic neutron scattering from a powder sample. In this study the dynamic structure factor $S(Q,\omega)$ was observed to be sensitive to superconductivity. In particular, a feature with energy transfer $\hbar\omega = 61$ meV, which could be

attributed to a motion of apical oxygen [O(4)] along the c axis, had a marked change in its Q dependence in the vicinity of T_c. Above and below T_c the Q dependence could be explained if the dynamical correlation length of this motion was short range. In the vicinity of T_c, $S(Q, \omega)$ had a stronger Q dependence which was successfully modeled as a divergence of this correlation length.

PDF studies of a variety of cuprate superconductors indicate that localized lattice instabilities associated with displacements of oxygen are widespread in these materials.[6] This behavior cannot be completely explained by steric incompatibilities in the structures. This point is discussed in detail in this paper. After discussing the observation and characterization of these distortions as they appear in $Nd_{2-x}Ce_xCuO_{4-y}$, we discuss a possible mechanism that could give rise to a strong coupling whereby the lattice distortions are stabilized by the electronic system. We also speculate on how such a coupling could give rise to high-T_c superconductivity.

The paper is laid out as follows. The technique used for extracting local structure information is relatively new and, hence, it is discussed in detail. In Sec. II the pair density function is defined as a fourier transform of the powder-diffraction structure function. In Sec. III we discuss in detail our data collection and analysis procedures. Structural information is extracted from the PDF by a refinement procedure which is analogous to the Rietveld refinement of powder-diffraction data. The method of calculating PDF's from structure models is defined and the procedures used for refining model parameters are described in Sec. IV. The experimental results and the discussion are all contained in Secs. V and VI. In Sec. V the model for the local structure of $Nd_{1.835}Ce_{0.165}CuO_{4-y}$ is presented. In Sec. VI we explore the implications of the observed local structure. A driving force for the distortions is proposed and we speculate on the role that they play in the mechanism for superconductivity.

II. PAIR DENSITY FUNCTION

The atomic pair density function $\rho(r)$ is a representation of the atomic structure of a material expressed in real-space units. The function $\rho(r)$ charts the probability of finding a second atom at a distance r from another atom. The function can be obtained from x-ray or neutron-diffraction data directly, without presuming any kind of structural model. This fact led to its widespread use for describing noncrystalline structures such as glasses and liquids.[16] Recently, it has been applied to crystalline and quasicrystalline materials.[17] In these materials its main usefulness lies in its ability to reveal features of the local structure of a material which are not reflected in its long-range structure. For example, this might be small displacements of atoms from their average crystallographic positions. These displacements are not ordered over long range but may be ordered over short range. This local order will be evident in the PDF but not in a crystallographic analysis which presumes a periodic structure. As we will discuss in this paper, refinement of the PDF is also useful for estimat-

ing short-range order parameters, such as thermal factors and structural correlation lengths, with better precision than is possible using crystallographic techniques such as Rietveld refinement of reciprocal space powder-diffraction data. In fact a "real-space-refinement" of the PDF and a "reciprocal-space" (or Rietveld) refinement of the diffraction data provide highly complementary information. To obtain the most information from powder-diffraction data, a joint PDF and Rietveld analysis is recommended.

In this section we define the PDF as a function of the total scattering function $S(Q)$, where $Q = |\mathbf{Q}| = |\mathbf{k} - \mathbf{k}_0|$ is the magnitude of the momentum transfer of a scattered particle. Here, $\mathbf{k}_0$ and $\mathbf{k}$ are the incident and scattered wave vectors, respectively. In the case of elastic scattering Q is given by $Q = 4\pi \sin \theta / \lambda$. In the next section we describe how the function $S(Q)$ can be recovered from neutron-powder-diffraction data.

After correction for absorption and multiple scattering, the intensity of neutrons scattered from a collection of atoms is given by[18]

$$I(\mathbf{Q}) = \left\langle \sum_{\alpha \alpha'} b_\alpha b_{\alpha'} \exp\left[i\mathbf{Q} \cdot (\mathbf{x}_\alpha - \mathbf{x}_{\alpha'})\right] \right\rangle , \qquad (1)$$

where b_α and $b_{\alpha'}$ are the neutron-scattering lengths of the αth and α'th atoms, respectively, at positions $\mathbf{x}_\alpha$ and $\mathbf{x}_{\alpha'}$. The angular brackets $\langle \rangle$ denote a time average. This intensity depends on the total number of scatterers present, their scattering strengths, and it contains a component of incoherent scattering. It is convenient to define a structure function $S(\mathbf{Q})$ which depends only on the structure of the sample. Thus,

$$S(\mathbf{Q}) = \frac{I(\mathbf{Q})}{N \bar{b}^2} - \frac{\overline{b^2} - \bar{b}^2}{\bar{b}^2}. \qquad (2)$$

Here N is the number of scatterers, and the bars denote averages over all the scatterers. The second term gives the incoherent scattering contribution.

The pair density function $\rho(r)$ is obtained from $S(\mathbf{Q})$ by spherically averaging and fourier transforming it. In detail[18]

$$S(Q) = 1 + \frac{4\pi}{Q} \int_0^\infty [\rho(r) - \rho_0] \, r \, \sin Qr \, dr, \qquad (3)$$

and

$$\rho(r) = \rho_0 + \frac{1}{2\pi^2 r} \int_0^\infty Q \, [S(Q) - 1] \, \sin Qr \, dQ. \qquad (4)$$

This expression yields the atomic structure in real-space units as an explicit function of a measurable scattering intensity.

A number of other correlation functions appear in the literature and are defined here for completeness. The "reduced radial distribution function," $G(r) = 4\pi r[\rho(r) - \rho_0]$. An alternative expression, often called the "pair distribution function,"[19] is $g(r) = \rho(r)/\rho_0$. Finally, a commonly used correlation function is the "radial distribution function" (RDF),[18] $f_{\mathrm{RDF}}(r) = 4\pi r^2 \rho(r)$. The RDF has the useful property that it can be used directly to

estimate the coordination number of an atom site. The integrated intensity under a given peak of the function yields the number of atoms in the coordination shell giving rise to that peak.

Information about lattice dynamics is contained in the inelastic scattering from a sample. It is thus of interest to examine explicitly the effect of accepting both elastically and inelastically scattered neutrons in our experiments. In a time-of-flight neutron experiment, inelastic scattering of all energy transfers $\hbar\omega$ are accepted, within the energy window of the experiment. If Q is independent of ω, the structure function obtained is the total structure function $S(Q)$ which is an integration, over all ω, of the dynamic structure function $S(Q,\omega)$. Only information from instantaneous scattering events is retained and the resulting PDF is a time average of instantaneous atom-pair correlations. There is no lattice dynamical information contained in the ideal $S(Q)$ function. However, in the real experiment the ideal $S(Q)$ is not recovered and some indirect information remains about the dynamics of the structure. This is because the integration of $S(Q,\omega)$, over ω, is imperfect. It does not extend to infinite energy transfers but is limited by the energy bandwidth of the experiment. Also, the integration is carried out, not at constant Q according to the definition of $S(Q)$, but at constant 2θ and constant time of flight. Thus, the intensity of inelastically scattered neutrons becomes shifted in the measured $S_{\mathrm{EXP}}(Q)$. The magnitude of this shift depends on the detector angle. Thus, a feature in $S(Q)$, or in the PDF, which depends on detector angle, is likely to be dynamic in origin. This will be discussed in more detail elsewhere.[20]

III. EXPERIMENT

A. Data collection

The experiments described in this paper were carried out using the Special Environment Powder Diffractometer (SEPD) at the Intense Pulsed Neutron Source (IPNS) at Argonne National Laboratory.[21] Two samples from the $\mathrm{Nd}_{2-x}\mathrm{Ce}_x\mathrm{CuO}_{4-y}$ family were considered. One had $x = 0.165$ and the other had $x = 0.2$. The sample preparation and characterization were carried out by Hinks and Dabrowski at Argonne National Laboratory and have been described elsewhere.[12] The samples were made by solid-state reaction of $\mathrm{Nd}_2\mathrm{O}_3$, CeO_2, and CuO. Both samples were annealed in flowing high purity argon at $900\,^\circ\mathrm{C}$ for 16 h. Superconductivity was measured using a superconducting quantum interference device magnetometer. The $x = 0.165$ sample had a superconducting onset at $T_c = 22$ K. The $x = 0.2$ sample had no bulk superconducting transition. A possible phase separation has been reported to occur in this system.[22] These compositions were chosen for this experiment since neutron diffraction indicated that they could be made single phase. No evidence of phase separation or impurities could be seen in x-ray, or subsequent neutron, diffraction patterns. Approximately ten grams of each sample was finely powdered in a mortar and pestle and loaded into a cylindrical, extruded, vanadium tube. The tubes were sealed with helium transfer gas at atmospheric pressure. They were then mounted on to a displex closed loop helium refrigerator. The sample was surrounded by two nested aluminum heat shields. The entire chamber containing the sample and refrigerator unit was evacuated.

The data collection method used for obtaining the PDF is essentially the same as that for any powder-diffraction experiment. Indeed it is possible to carry out a conventional crystallographic analysis and a PDF analysis *on the same data*. However, the data collection regimen is stricter when a precise PDF is desired. This is because the absolute $S(Q)$ must be obtained by making quantitative corrections and carrying out an absolute normalization. Thus, the data must be collected with very good statistics. Furthermore, the success of the fourier transform depends on data being collected to large values of Q. A rule of thumb[17] is $Q_{\max} \geq 3\sigma_{\mathrm{DW}}$, where σ_{DW} is the standard deviation of the Debye-Waller attenuation of the Bragg intensity; the Debye-Waller function is defined as $M = \exp\left(-\frac{1}{2}Q^2/\sigma_{\mathrm{DW}}^2\right)$. For a crystal at low temperature, $3\sigma_{\mathrm{DW}}$ can be as high as 45 Å^{-1}, and is generally higher than 30 Å^{-1}. In comparison, a typical Rietveld refinement will be carried out up to $Q \approx 10$–$12\ \text{Å}^{-1}$. The high-Q information originates from short-wavelength, high-energy, particles. These are most sensitive to small atom displacements and provide a lot of information about the local structure. They are abundantly available from a pulsed neutron source, which has a large flux of epithermal neutrons.

Detectors are grouped into banks which are centered at $2\theta = 150^\circ, 90^\circ, 60^\circ, 30,^\circ$ and 15°, where 2θ is the scattering angle. Neutron wavelengths are determined by the time-of-flight method.[21] The neutron flight path for the SEPD instrument is $L_0 = 14$ m, $L_1 = 1.5$ m, where L_0 is the length of the incident flight path and L_1 is the length of path for the scattered neutrons. Data are collected from $t_t = 1000$ μs to $t_t = 30\,000$ μs, where t_t is the time of flight. This gives a $Q_{\max}$ of ≈ 46 Å^{-1} for the banks situated at $2\theta = 150^\circ$. Data collection from powder samples using the SEPD has been described elsewhere.[21] In this paper we outline aspects of our data collection and analysis regimen that are important to obtain precise PDF's.

In order to make accurate corrections to the measured sample scattering, extra data must be collected. An experiment is run to determine the instrumental background, including scattering from the sample environment chamber. For instance, in the case of low-temperature measurements, the sample environment will be a displex helium refrigerator mounted with all of the heat shields in place. A separate experiment is carried out to measure the scattering from the empty sample container. Again, this measurement is carried out with the container mounted with the full sample environment in place. However, even if the sample is to be measured at low temperature, negligible errors are introduced if these characterization runs are carried out at room temperature. Finally, in order to characterize the source spectrum and the detector efficiency, data are collected from a reference sample. A solid rod of vanadium is used, with no special environment. The data collection regimen is summarized in Table I.

TABLE I. Summary of the data collection regimen for determining an accurate PDF of a sample.

Name	Intensity label	Environment[a]	Container[b]	Sample
Sample run	I_s	yes	yes	powder specimen
Can run	I_c	yes	yes	no
Background	I_b	yes	no	no
Vanadium	I_v	no	no	vanadium rod

[a]Environment can be a displex refrigerator, an automatic sample changer, or any other device such as a furnace or a pressure cell.

[b]Usually a thin walled, extruded, cylindrical vanadium canister is used.

Data must be collected with good statistics. A procedure for estimating the optimum collection time has been discussed.[17,23] Data were collected from the $Nd_{2-x}Ce_xCuO_{4-y}$ samples for a duration of $\approx$ 4 h per temperature, over a range of temperatures from 50 K to 10 K. This yielded an integrated intensity, over the full range of $S(Q)$, in excess of 5×10^7 counts. Background and reference sample data are smoothed during data processing and do not require such good statistics. These data were collected for $\approx$ 1.5–2 h per experiment.

B. Data analysis

The goal is to obtain the PDF of a sample from the neutron diffraction experiment described in Sec. III A. The formula for $\rho(r)$ is given in Eq. (4) in terms of the single-scattering, coherent, structure function $S(Q)$. This function depends only on the structure of the sample and assumes an ideal diffraction experiment. The experiment must be carried out in the so-called "no scattering" limit. There is no sample absorption or multiple scattering, and no extraneous scattered intensity from the sample container or apparatus. The strategy for data collection described in Sec. III A is designed to allow the single-scattering structure function to be recovered from real data as accurately as possible. Data are analyzed using the analysis package called GLASS. The data analysis procedure has been described in detail elsewhere,[24,25] and will be summarized here. The data sets required for accurate data reduction are listed in Table I. Initially the instrument background is subtracted from the sample, reference, and empty can data sets. At this point a delayed neutron background is also explicitly subtracted from these data. The delayed neutron background emerges from the uranium target and forms a constant background current which is a fixed proportion, $p_{dn} \approx$ 3–5 %, of the total scattered flux. The incident spectrum decays to the delayed neutron intensity at long time of flight and this background can be subtracted with some certainty. For a given neutron target this proportion does not change and values can be transferred from experiment to experiment without introducing significant error.

The absorption correction $A_1(\lambda)$ and multiple-scattering contributions to the structure function S_m can be calculated for cylindrical geometry samples. The procedure used is due to Price[24] following Blech and

Averbach.[26] This correction takes into account the absorption and multiple-scattering from the sample, and the sample container. Each data set is multiplied by the absorption correction factor and the multiple-scattering contribution to the total scattering is subtracted. A Placzeck correction[27] is calculated to correct distortions to the data due to neutrons that have been inelastically scattered by phonons. The method relevant to our experiment has been described in detail.[24,28] This gives rise to an additional correction term, S_p. It should be noted that if a strongly Q-dependent feature appears in the inelastic scattering, for instance, an excitation with a well-defined momentum, then these sharp, features of dynamic origin still appear in $S(Q)$ even after the Placzek correction, which only accounts for inelastic scattering within the ballistic approximation. The experimental intensity, corrected for absorption, and after subtracting the contribution from the empty can, is then

$$I_{EXP} = TN\phi(\lambda)\,\Delta\lambda\,\eta(\lambda)[\,\overline{b}^2 S(Q) + (\overline{b^2} - \overline{b}^2)$$
$$+\overline{b}^2 S_p + \overline{b}^2 S_m], \qquad (5)$$

where T is the total time of the measurement, $\phi(\lambda)\,\Delta\lambda$ is the incident flux, and $\eta(\lambda)$ is the detector efficiency. The total number of scatterers in the beam is given by N. As mentioned, S_p and S_m are explicitly calculated. The data must thus be corrected to account for the incident spectrum and detector efficiencies. The most accurate way to do this is by using a measured vanadium reference data set. The source spectrum and detector efficiencies are sample independent. Thus the ratio of intensities from the sample and from the vanadium rod will be independent of spectral and detector efficiency effects. Vanadium is an almost completely incoherently scattering sample and $S_{VAN}(Q) \approx 1$. The small amount of coherent scattering in the vanadium data is corrected by smoothing to remove the residual Bragg peaks.

Finally, the intensity is normalized by the number of scatterers. In principle, N can be determined from the density and volume of the sample that is in the beam. In practice, this is not known precisely and the sample density can be varied as a parameter to obtain a correct normalization. This is ensured when the average structure function, $\overline{S(Q)} \rightarrow 1$ and the absolute value of $S(Q) \rightarrow 1$ as $Q \rightarrow \infty$.

Once $S(Q)$ has been determined, the sample PDF can be found by a direct Fourier transform, according to

Eq. (4). For improved statistics on the data, but at the expense of Q resolution the $S(Q)$ from different data banks can be combined. They should not be combined before this point because the θ-dependent Placzek correction must be applied independently to each bank.

A mild damping function can be applied to the data in the high-Q region. This forces the intensity of $[S(Q) - 1]$ to approach zero smoothly at the finite-Q cutoff of the Fourier transform. This reduces high-frequency oscillations in $\rho(r)$ at low r; however, it increases the broadening due to finite Q termination. If data are collected over a wide enough range of Q, then the spurious oscillations are small and the use of damping is not required. In the current experiments the data were terminated at $Q_{max} = 35$ Å^{-1}. The data for $Q \geq 33$ Å^{-1} were mildly damped by multiplying them by the function $D(Q) = \cos^2\left(\frac{\pi}{2}\frac{(Q-Q_c)}{(Q_{max}-Q_c)}\right)$, where Q_c is the cutoff for the undamped data; i.e., $Q_c = 33$ Å^{-1} and $Q_{max} = 35$ Å^{-1} in the current case. The structure function obtained from the $x = 0.165$ sample data, collected at 10 K, is shown in Fig. 1(a), expressed as $Q[S(Q) - 1]$. Figure 1(b) shows the resulting PDF over a wide range of r. The solid line is from the data. The dotted line is the calculated PDF from the T' structure. This illustrates that PDF's can be obtained by this procedure which are quantitatively accurate to beyond 20 Å in r. This is the only technique that can reveal direct structural information on these mesoscopic length scales.

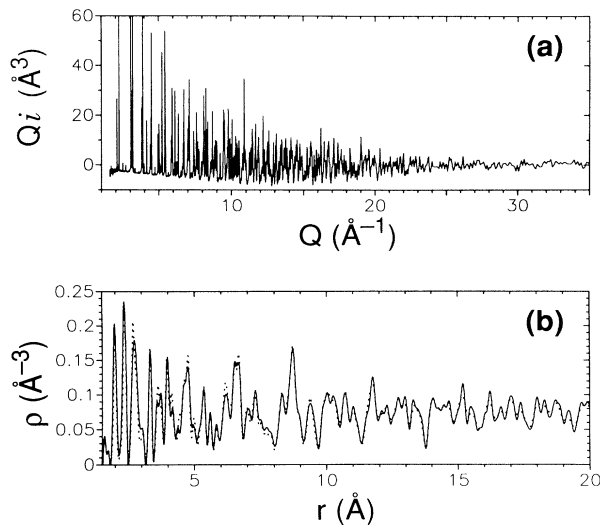FIG. 1. (a) Scattering function $Qi(Q) = Q[S(Q)-1]$ from Nd$_{1.835}$Ce$_{0.165}$CuO$_4$ data taken at 10 K. The Bragg peaks at low Q are cutoff in the figure. They extend to a height of ≈ 150 Å^3. (b) Solid line: the resulting PDF after fourier transforming the data in (a). Dotted line: model PDF based on the T' structure. This illustrates the accuracy that is possible, even to 20 Å and beyond in r, in data PDF's using the data aquisition and analysis procedures described in the text (Ref. 6).

IV. STRUCTURAL MODELING USING THE PDF

Structural information can be extracted from the PDF by refining a structure model in analogy with the Rietveld refinement of powder-diffraction data. Standard crystallographic refinements are carried out on data expressed in reciprocal space. In contrast, the PDF is a representation of the data in real space and, thus, we refer to refinements of this function as real-space refinements. The relationship between these two analysis procedures is illustrated schematically in Fig. 2. The refinements are carried out by iterating the loops until a minimum is found in a residuals function which expresses the agreement between the data and model functions. In a reciprocal-space refinement the position and intensity of Bragg reflections are analyzed. These contain information about the periodicities in the structure and the resulting structure model represents a periodic average of the sample structure. It reflects the long-range atomic order present in the material. This will be referred to as the "crystal structure" since the essence of a crystal is its periodicity. The PDF is a fourier transform of all of the single-scattering intensity, including Bragg and diffuse scattering. It thus gives information about both long, and short, range order in the material. This structure will be referred to as the "atomic structure" of the material to differentiate it from the crystal structure defined above. In practice, most useful information in the PDF occurs in the range up to ≈ 20 Å and, thus, this function gives most information about the short- to medium-range order in the material. In simple crystals the short- and long-range order will be the same. However, this need not necessarily be the case and in complex crystals the crystal structure does not necessarily give a good description of the local environment of ions. In this case, a refinement
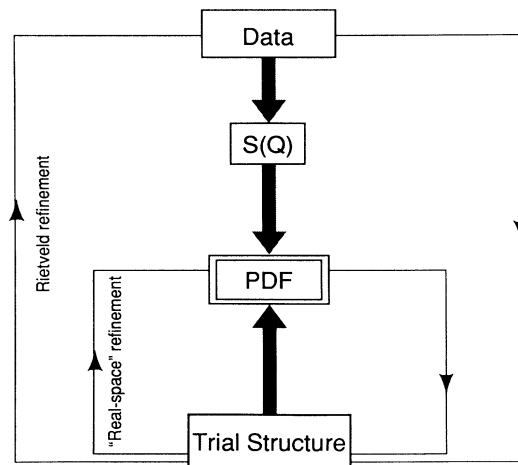

FIG. 2. Flowchart illustrating the relationship between structure refinement procedures. The large loop is iterated in a Rietveld refinement, the small loop is iterated in a refinement of the pair distribution function. The large loop yields the periodic crystal structure. The small loop yields, predominantly, the local atomic structure.

of the sample PDF may reveal new information.

In this section two methods of refining structural models from the PDF are described. Structure parameters are refined by a process of minimizing an agreement factor, or A factor. This is defined first. Then there is a discussion of how a PDF can be calculated from a structure model. These calculated PDF's will be referred to as model PDF's to distinguish them from experimentally derived PDF's which will be called data PDF's. Finally, the two refinement procedures that we used will be explained.

A. Agreement factor

The A factor[23] is defined as

$$A = \left\{ \frac{\int [\Delta(r)]^2 \, dr}{\int dr} \right\}^{\frac{1}{2}}, \tag{6}$$

where the difference function $\Delta(r) = [\rho^{mod}(r) - \rho^{dat}(r)]/\rho_0$: ρ^{mod} is the PDF of the model, ρ^{dat} is the PDF from the data, and the integrals are over any specified range of r. The A-factor function is a sum of squares of residuals which directly parallels the R factor used in crystal structure refinements.[29] However, there is not complete correspondence between them and the properties of the R factor are not transferable in whole to the A factor. In particular, it is not trivial to extract a meaningful χ^2 value from the A factor because of statistical correlation of points in the PDF. A procedure has been described that can yield a good estimate of reduced χ^2 using[25]

$$\chi^2 = \frac{A^2}{A_{MIN}^2}, \tag{7}$$

where A_{MIN} is the minimum A factor, or the expected A factor if the model perfectly described the structure of the experimental sample. The value derives from the random errors of the experimental data. It is given by the average standard deviation of random errors on the points in the PDF over the range of interest. These random errors can be estimated from the experimental data by a direct error propagation technique.[23] Statistical correlations of points in the PDF are taken into account by adjusting the number of observations in the PDF in a controlled way.[25]

B. Calculating the model PDF

The PDF of the trial structure is calculated according to

$$\rho(r) = \frac{1}{N} \sum_{k,l=1}^{N} \frac{b_k b_l}{\overline{b}^2} \, \delta(r - r_{k,l}), \tag{8}$$

where the sums are over all N atoms. Atoms in the pairs are separated by $r_{k,l} = |\mathbf{r}_k - \mathbf{r}_l|$, where $\mathbf{r}_m$ is the specified position of the mth atom, and the δ is the Dirac delta function. The weighting factor accounts for the difference in the scattering length of the atoms in the pair with respect to the specimen average scattering length.

Thus, b_m is the scattering length of the mth atom in barns and $\overline{b}$ is the mean scattering length for the sample. The normalization ensures that the average pair density equals the number density of the sample, $\overline{\rho(r)} = \rho_0$.

Harmonic atom motion in the crystal is approximated by convoluting the δ functions with normalized Gaussian functions defined by,[23]

$$b(r) = \frac{1}{\sqrt{2\pi}\sigma_C} \exp\left[-\frac{1}{2}\left(\frac{r^2}{\sigma_C^2}\right) \right]. \tag{9}$$

The Gaussian standard deviation σ_C is a parameter which can be refined by fitting the model to the experimentally determined PDF. The main contribution to σ_C is the quantum zero point and thermal motion of the ions in the sample; we will denote this σ_S. There is also an r-dependent contribution σ_2 due to the finite width of the diffraction peaks. The total broadening is given in our modeling by[23]

$$\sigma_C = \sigma_S + \sigma_2 \, r^2. \tag{10}$$

The sample dependent contribution σ_S is directly related to the crystallographic thermal factors. For the case of a single, isotropic broadening for all the atom sites in the structure, the isotropic thermal parameter, B, is given by $B = 4\pi^2\sigma_S^2$, where B is defined in the Debye-Waller factor, $F_{DW}^2 = \exp\{-2BQ^2\}$.[18]

For the case of site-dependent anisotropic thermal broadening, the relationship can be made as follows. Let $\mathbf{r}^{\alpha\alpha'}$ be the vector joining the average position of atom α to the average position of atom α'. The value of σ_S required to broaden the pair correlation of these two atoms is given by

$$\sigma_S^2 = (\sigma_r^\alpha)^2 + (\sigma_r^{\alpha'})^2, \tag{11}$$

where σ_r^α is the uncertainty in the position of atom α projected onto the direction of the vector $\mathbf{r}^{\alpha\alpha'}$. The uncertainty, σ_r^α, can be estimated from

$$(\sigma_r^\alpha)^2 = \frac{1}{|\mathbf{r}^{\alpha\alpha'}|^2}\left\{ (r_1^{\alpha\alpha'})^2 \, U_{11}^\alpha + (r_2^{\alpha\alpha'})^2 \, U_{22}^\alpha \right.$$
$$\left. + (r_3^{\alpha\alpha'})^2 \, U_{33}^\alpha \right\}, \tag{12}$$

where $r_i^{\alpha\alpha'}$ are the components of $\mathbf{r}^{\alpha\alpha'}$ and U_{ii}^α are the standard crystallographic anisotropic thermal parameters which are defined in the usual way: $F_{DW}^2 = \exp(-2\pi^2 [h^2 a^{*2} U_{11} + \cdots])$. The U_{ii} correspond to the mean-square atom displacements when the atomic motion is modeled as being harmonic. Thus, by refining the Gaussian broadening in the PDF, estimates of the anisotropic thermal parameters are possible.

When refining atom displacements, fewer thermal parameters are used. This is to prevent thermal broadening parameters from becoming correlated with atom displacement parameters, and also to keep the number of refinable variables to a minimum. In this case, σ_S is described by two parameters:

$$\sigma_S = \sigma_0, \qquad r < r_c$$
$$= \sigma_1, \qquad r_c < r.$$

The first parameter σ_0 is used for the low-r region of the PDF which contains atom-atom correlations between directly bonded atoms. The motion of these atoms is correlated. Thus, the atoms in these pairs move cooperatively and in the instantaneous PDF their pair correlation will have a narrow distribution. Thus a small broadening parameter may be required to explain nearest-neighbor peaks in the PDF. The motion of pairs of atoms that are not directly bonded to each other is virtually uncorrelated. Thus for atom-atom pairs which are not direct neighbors, a larger value, σ_1 is defined. In the model, a cutoff radius, r_c is specified. Atom pairs below r_c take σ_0; atom pairs above r_c take σ_1.

C. Refinement of thermal factors

The first real-space refinement technique that will be described uses the method of steepest descent (MOSD) to minimize the A factor.[30] Using this approach, anisotropic thermal parameters, site occupancies, and atom displacements can be refined. As already discussed this is not the preferred method for finding structures of locally displaced atoms. However, it is a valuable first step for establishing which atoms, if any, appear to be displaced in the structure, and in which directions.

This refinement approach has also shown that it can refine thermal parameters with good accuracy. Values can be obtained that are close to those expected based on the probable lattice dynamics of the sample.[31] The reason that this technique can yield accurate values for thermal parameters is because of the range of Q over which data for the PDF is collected. This range is $\approx$ 2–3 times σ_{DW}, the standard deviation of the Gaussian Debye-Waller envelope. A value for σ_{DW} can be estimated for a prototypical crystal. Using a Debye temperature $\Theta_D = 300$ K and mean atomic weight of 60 g/mol, the zero point mean-square displacement, $\langle u^2 \rangle_0 = 20$ pm^2 and $\sigma_{DW} \sim 16$ Å^{-1} at low temperature. Most Rietveld refinements are terminated at $Q \approx 12$ Å^{-1}, which is much less than one σ_{DW}. An estimate of the width of the Gaussian from data over this range will be quite uncertain. Furthermore, in Rietveld refinements, the thermal parameter often becomes significantly correlated with other variables such as occupancy factors, absorption, and scale factor parameters. Finally, if any static atom displacements are present in the material, which are not ordered over long range, the effect of these will be included in the Rietveld refined Debye-Waller factor. In the PDF these two factors are less correlated and can be differentiated to a large degree. A large thermal motion amplitude gives rise to a symmetrical peak broadening, whereas, static displacements will shift intensity. This is discussed in more detail in Sec. V. Thus, MOSD refined thermal factors are more to be believed than those obtained from a Rietveld refinement. A detailed analysis of a material with a well known structure, and well known lattice dynamics, is needed to investigate this in more detail.

The A factor is minimized using a linearized least-squares approach; the method of steepest descent.[30] It has been found that refined values can be reproduced very readily, even when the refinement is started with quite different initial values, yielding physically reasonable values. This procedure has proven very robust when refining anisotropic thermal factors.

D. Refinement of atom displacements

When refining atom displacements a Monte-Carlo simulated annealing (MCSA) procedure[32] is preferred for minimizing the A factor. This method is able to sample a greater volume of the model parameter space before settling into an A-factor minimum. Thus, it is less likely to get trapped in a false minimum than a procedure that samples less of the parameter space. The refinement is given a high initial temperature. Thus, early in the refinement it is able to sample a wide range of the parameter space, even if a worse agreement is temporarily obtained. As the refinement goes on the temperature is lowered and the program gradually settles into the best A-factor minimum. The program used is called MONT and was developed by Toby.[33] The program works as follows. An initial structure model is specified. Certain atom displacements are then deconstrained and these are the refinable variables. These are then individually varied in a succession of Monte-Carlo steps. First, one of the variables is selected at random. The magnitude of the displacement α given to the selected variable is also determined randomly, but must lie in the range $-\delta_{max} < \delta < \delta_{max}$; where δ_{max} is specified and is the maximum displacement allowed for that variable. The model PDF is recalculated and the new A factor evaluated. The displacement is then either accepted or rejected as a permanent modification to the model. The decision is made randomly but weighted by a probability for acceptance of

$$P = \frac{1}{1 + \exp(\frac{\delta A}{T_M})}, \tag{13}$$

where δA is the change in the A factor; T_M is the Monte-Carlo annealing temperature. The process is then iterated. As the refinement proceeds, δ_{max} is automatically varied to keep the percentage of accepted steps at around 50%. This maintains the efficiency of the program and ensures that a suitable range of the parameter space is being probed. The program is considered to have equilibrated when the number of accepted steps which improve the A factor is approximately equal to the number of accepted steps that worsen the A factor. At this point the annealing temperature is reduced by a factor of 2 and the process begins again. In this way the program systematically freezes the model into an A-factor minimum. The program terminates when the temperature is so low that changes in the A factor over 100–1000 steps are below a threshold limit.

The simulated annealing temperature should be high enough initially so that $T_M > \sigma(A)$, where the $\sigma(A)$ is the standard deviation of the A factor. This depends on the counting statistics of the data and can be evaluated directly.[25] The lower threshold limit for δA, at which the program terminates the refinement, is arbitrarily specified. The smaller it is, the closer the model parameters

will come to their best estimate, but at the expense of increased computation time.

The initial atom positions are input in a unit cell. The internal symmetry of the model unit cell can be modified as desired and changes in symmetry can be applied to specified sublattices. For instance, as will be discussed, in the current modeling it was found that the copper and neodymium sublattices were not distorting and these retain the full crystallographic symmetry. On the other hand, oxygen is displaced off its special positions. Thus, all symmetry operations were removed from the oxygen sublattice so that each oxygen position in the cell could be treated independently. The modeling process then consists of identifying possible atom displacements, and refining them. The number of variables must be kept to a minimum for the results of the modeling to be meaningful. Thus possible patterns of ordered displacements are identified. The variables are then constrained to reproduce this pattern. The best models are arrived at by systematically modifying the input, and constraining displacements, until physically meaningful patterns of displacements, described by only a few variables, yield a good agreement.

V. LOCAL STRUCTURE OF $Nd_{2-x}Ce_xCuO_{4-y}$

A. Evidence for atom displacements

In this section, the PDF is examined for evidence of significant displacements of atoms from their average crystallographic positions. Initially, PDF's of models based on the T' crystal structure are compared to the data PDF. A significant improvement in χ^2 is obtained when certain atom displacements are introduced. It is found that the deviations from the periodic structure are too extensive to be attributed to local distortions about dopant impurity ions. In particular, it is clear that significant displacements of O1 (in-plane oxygen) are present in directions perpendicular to the Cu—O bond. Similar displacements of O2 (out-of-plane oxygen) are also present. There is no evidence of significant positional disorder at the copper or neodymium sites beyond expected thermal motions. It should also be noted that there are no significant displacements of O1 observed parallel to the Cu—O1 direction. To first order the Cu—O nearest-neighbor (NN) bond length is not changing and we conclude that in-plane copper breathing, or quadrupole, distortions are not present, even on the local level.

$Nd_{2-x}Ce_xCuO_{4-y}$ takes up the T' structure.[34,35] This structure, shown in Fig. 3, referred to the conventional T' unit cell. The space group is $I\,4/mmm$. For cerium content, $x = 0.165$; $a = b = 3.951$ Å; $c = 12.090$ Å.[22] It is necessary to consider enlarged unit cells when symmetry breaking atom displacements are introduced into structural models. Two of these have been used in the current modeling and these are referred to as the root-2 ($R2$) cell and the 2×2 cell. The $R2$ cell is rotated by 45° about **c** with respect to the T' cell, and $|a_{R2}| = |b_{R2}| = \sqrt{2}\,|a_{T'}|$. The 2×2 cell has axes parallel to the T' cell axes but the cell has been doubled along the a and b directions. In
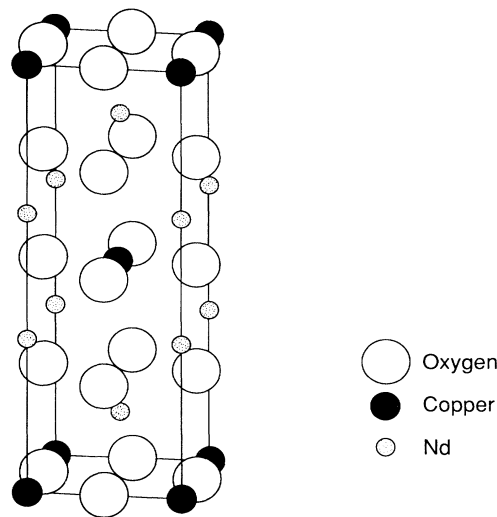

FIG. 3. Illustration of the T' structure.

both cases the c axis is unchanged.

It is useful to establish some facts about the relative position of atoms in the T' structure. The copper is in square planar coordination with four oxygen ions at a distance of 1.97 Å from it. These "CuO_4 plaquettes" form an infinite corner shared network which is the "CuO_2 plane." There is no anion directly above or below the copper which lies on a center of symmetry.

Neodymium and cerium form a solid solution by randomly occupying the M sites. In the T' cell there are four M atoms but all the M sites are symmetry equivalent. They sit inside a cuboid of eight oxygen ions. The packing is analogous to that in the fluorite structure except the cube, with anions at the corners, is elongated into a cuboid and the M atom moves away from the center. It is closer to the four out-of-plane oxygens (O2) than to the in-plane (O1) ions because of the presence of the copper. Oxygen ions lie one above another along the c-direction forming continuous $\cdots$—O1—O2—O1— $\cdots$ rods. In contrast to the La_2CuO_4 structure, each O2 ion cannot be exclusively associated with a particular CuO_2 plane. In the T' structure each O2 lies symmetrically between CuO_2 planes and is equally shared between adjacent planes.

Crystallographic models based on the T' cell were compared to our data PDF's. First a Rietveld refinement from the literature was considered. The parameters of Kwei et al. were used.[36] They refined neutron-powder-diffraction data from a sample of $Nd_{2-x}Ce_xCuO_{4-y}$, $x = 0.15$, taken at 10 K. The thermal factors are reproduced in Table II. These values are consistent with other crystallographic refinements.[22,37] The values are large; in particular the values refined on the oxygen sites which range from $\approx$ 37–70 pm^2. This indicates the probable presence of static, or quasistatic, displacements of these ions in the material.

The PDF was calculated from this Rietveld-refined model and compared to the 10-K data PDF of our

TABLE II. Anisotropic thermal parameters. (a) Values published by Kwei et al., Phys. Rev. B **40**, 9372 (1989) from a Rietveld refinement of an x=0.15 sample. (b) Refined using the MOSD real-space-refinement technique on the data PDF from the x=0.165 sample. Both sets of data were collected at 10 K. U_{ii} is defined in Sec. IV B.

		(a) Kwei et al.[a] (pm^2)	(b)MOSD approach[b] (pm^2)
M	$U_{11}=U_{22}$	16.3	11.4
(0,0,0.3525)	U_{33}	21.5	10.0
Cu	$U_{11}=U_{22}$	28.0	12.2
(0,0,0)	U_{33}	41.1	19.1
O1	U_{11}	56.6	35.7
$(0,\frac{1}{2}0)$	U_{22}	36.5	15.7
	U_{33}	69.6	43.1
O2	$U_{11}=U_{22}$	45.7	21.6
$(0,\frac{1}{2},\frac{1}{4})$	U_{33}	48.4	34.2

[a]A factor over range $1.8 < r < 10.0$ Å: A=0.209.
[b]A factor over range $1.8 < r < 10.0$ Å: A=0.138.

$x = 0.165$ sample. Over the range 1.8–10 Å, the agreement is A=0.209 ($\chi^2 = 23.2$). The Rietveld-refined model PDF is shown in Fig. 4 as a solid line, superimposed over the data (dotted line). This model PDF has much broader features than the data PDF and it is clear that the Rietveld-refined thermal parameters are a significant overestimate of the real quantum and thermal motion of atoms in the material.

A real-space refinement was carried out on the same data PDF. Anisotropic thermal factors were refined on every site using the MOSD procedure. The symmetry of the $I\,4/mmm$ space group and the atom positions of the T' structure were retained. The values $a = b = 3.951$ Å, $c = 12.1$ Å, were used and the M site was positioned at $z = 0.3525$. The agreement factor over the range $1.8 < r < 10.0$ Å is A=0.138 ($\chi^2 = 10.1$). The real-space-refined model PDF is reproduced in Fig. 4. The values refined for the anisotropic thermal factors are given in Table II. The shapes of the thermal ellipsoids are qualitatively similar to those of Kwei et al.;[36] however, the magnitudes are considerably smaller in the real-space refinement. This is reflected in Fig. 4. The features of the real-space-refined model PDF (dashed line) are sharper and better resolved than those of the Rietveld-refined model (solid line).

It would appear that the real-space-refined thermal parameters are more physically meaningful for describing the motion of atoms in the material. Nonetheless, a number of factors indicate that a complete description of the local structure must include some static, or quasistatic, atom displacements. First, we observe that refined thermal parameters on the O1 sites in directions perpendicular to the Cu—O bond (U_{11}, U_{33}) are still large: $U_{11} = 36$ pm^2 and $U_{33} = 43$ pm^2, compared with $U \approx 10$–20 pm^2 on copper and neodymium sites. A large mean-square displacement for the motion of the out-of-plane, O2, ion parallel to c is also refined. Thus, it seems clear that local
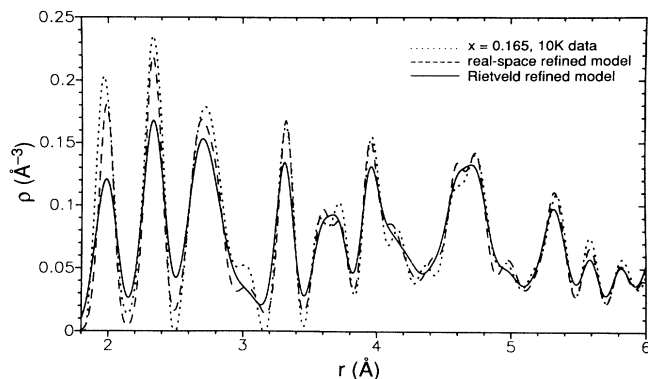

FIG. 4. Comparison of real space refined, and Rietveld-refined model PDF's for the T' structure. These are superimposed over the data PDF from the $x = 0.165$, 10 K, data.

static, or quasistatic, atom displacements are present on these ions in these directions. The other refined thermal factors are small and probably reflect the real quantum and thermal atomic motion. Slightly large values for copper parallel to c and O2 parallel to the ab plane may also indicate a small amount of displacive disorder of these ions in these directions. The degree of displacive disorder associated with these latter ions may simply be due to the presence of cerium dopant ions in the structure, as will be discussed.

Further, qualitative, evidence for atom displacements exists in the PDF. This can be understood by comparing Fig. 5 with Fig. 4. Figure 5 contains three model PDF's based on the T' structure. The dotted line is from the undistorted T' structure. The solid and dashed lines are from models in which oxygen ions have been
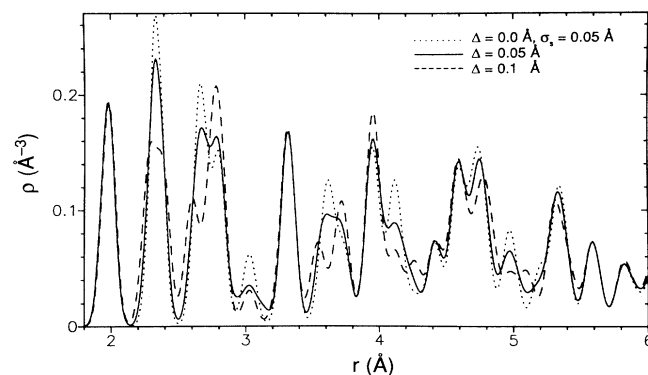

FIG. 5. Model PDF's, based on the T' structure, showing the effect on the PDF of introducing atom displacements into the model. The dotted line is the undistorted T' model PDF. The solid and dashed lines are from models in which all oxygen ions have been displaced parallel to the c axis by $\pm\Delta$ in an uncorrelated fashion. Compare this figure to Fig. 4 to see the effect on the PDF of, respectively, introducing static atom displacements vs increasing thermal motion parameters.

displaced from their equilibrium positions by $\pm\Delta$ parallel to c. This figure illustrates the effect on the PDF of introducing atom displacements in contrast to Fig. 4 where the effect of increasing the amplitude of atomic oscillation can be seen. One dramatic effect of displacing oxygen is to change the relative heights of the PDF peaks at 3.55 and 3.75 Å (Fig. 5). Increasing the amplitude of oxygen motion reduces the intensity of the 3.55 Å peak, but it cannot redistribute the intensity between these two peaks. The shape of the data PDF in this region is strongly suggestive that, on a local level, significant oxygen displacements are present.[38] Similar arguments apply to features elsewhere in the PDF. For instance, the peaks at 4.2 and 4.4 Å are shifted, but not broadened, in the data with respect to the T' model PDF. There is strong evidence in the PDF of significant displacements of oxygen from the average T' positions.

B. Cerium substitutional defect

In this section we establish that the observed oxygen displacements cannot be explained simply as lattice relaxations around dopant impurity ions. In $Nd_{1.835}Ce_{0.165}CuO_{4-y}$, one in twelve of the Nd^{3+} ions is replaced by a Ce^{4+} ion. The ionic radius of Nd^{3+} is 1.12 Å and that of Ce^{4+} is 0.97 Å.[39] The lattice around these smaller, more highly charged, dopant ions will relax with accommodating ion displacements. A static-lattice-energy minimization has been carried out to estimate the magnitude of these relaxations and will be described in detail elsewhere.[40] The results pertaining to the lattice relaxation around cerium are summarized here.

The cage of eight anions immediately surrounding the cerium ion collapses towards it with overall displacements of 0.066 Å for the four O1 ions, and 0.093 Å for the O2 ions. Both O1 and O2 displaced by 0.06 Å parallel to z. O2 also displaces 0.07 Å perpendicular to z while the in-plane relaxation of O1 is minimal. As might be expected, the O2 suffers the greater disturbance because it sits closer to the M site than does O1. No other ion in the structure is displaced by more than 0.03 Å. Nearby Nd and Cu ions displace fractionally away from the dopant ion, presumably because the Coulombic repulsion of the extra charge on the cerium is not fully screened by the surrounding anions. Nearby oxygen ions also become slightly displaced. However, apart from the cage of nearest-neighbor oxygen ions, the relaxations of ions in the structure are too small to be separated from the dynamic disorder of the solid in the PDF. For the purposes of calculating a model PDF for comparison with the data, the defect can be considered to be localized to the cluster of eight oxygen ions surrounding the cerium ion.

A model PDF was then calculated, based on the T' structure but containing relaxed cerium defects. The model was constructed as follows. The enlarged root 2 cell was used. This contains eight M sites. In order to retain the correct stoichiometry a cerium ion was placed on one of the sites with $\frac{2}{3}$ occupancy. A neodymium ion was also placed on the same site with $\frac{1}{3}$ occupancy. The

remaining M sites were filled with Nd ions. The eight oxygen ions surrounding the cerium site were partitioned in the same way. The ions with $\frac{2}{3}$ occupancy were displaced by the values indicated. The oxygens on the same site with $\frac{1}{3}$ occupancy were not displaced. In this way the magnitudes of the displacements, and the number of displacing ions, would be consistent with the lattice calculation.

The model PDF from this model is shown, superimposed on the data from the $x = 0.165$ sample at 50 K, in Fig. 6. A single thermal factor, $U_{ii}=12.5\,pm^2$, has been used on every site. The PDF of the undistorted T' structure, broadened with the same universal thermal factor, is also shown for comparison. It is clear from the figure that the displacements introduced by the defect improve the T' model. The agreements over the range $1.8 < r < 10.0$ Å are, for the undistorted T' structure, A=0.217 ($\chi^2 = 25.0$), and for the cerium defect model A=0.168 ($\chi^2 = 15.0$). The introduction of the relaxed cerium defect improves the model, but it cannot explain all of the atom displacements that are apparent in the PDF, as is evident, for example, by considering the labeled peaks in Fig. 6. All these peaks originate from atom pair correlations involving oxygen. The pair of peaks around 3.6 Å, labeled A, are particularly sensitive to the displacement of oxygen, as was discussed in Sec. V A. It is clear that even the presence of the relaxed cerium defects in the structure cannot explain the relative heights of these two peaks. There must be additional ion displacements present in the structure.

It is unlikely that the defect calculation severely underestimated the magnitude of the atom relaxations. The calculation was based on an ionic model and ignored shielding effects of the carriers in the system. This effect will be small because of the low density of carriers, but would tend to reduce rather than increase ion displacements, especially at larger distances from the defect. If anything we can expect the defect to have even less of an extent than the calculation predicts. Indeed,
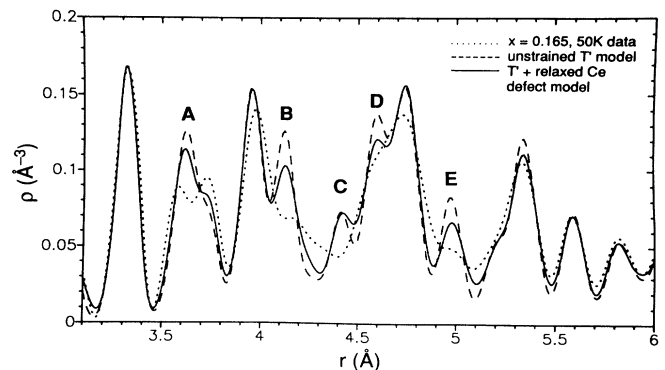

FIG. 6. Model PDF of the T' structure with a relaxed cerium defect (solid line) superimposed on the data PDF of the $x = 0.165$ sample (dotted line) from the data taken at 50 K. The model PDF from the undistorted T' structure (dashed line) is also shown for comparison. The labeled peaks are discussed in the text.

the thermal parameters refined from the PDF indicate that there is no significant displacive disorder associated with M sites. The calculated displacements of ions which sit beyond the first coordination shell of cerium must be considered as maximum values.

It is also significant that the calculation predicts larger displacements on the O2 site than on the O1 site. This is expected since the M-O2 distance is shorter than the M-O1 distance, thus, the O2 ions will experience the greater disturbance when a cerium ion is introduced. However, structure refinements, in real *and* reciprocal space indicate that a larger amount of displacive disorder is associated with the O1 site than the O2 site. The relaxed cerium defects are present; however, these cannot explain all of the displacive disorder observed in the PDF. In particular, additional displacements of O1 must be present. Further displacements of O2 ions are also likely.

C. Displaced ion structures

In this section, various displaced ion models are investigated. Since the approximation of periodicity has been relaxed, the number of possible structure models becomes immense. Thus, our goal in this modeling was to identify the essential features of the local structure of this material rather than necessarily establishing the perfect model.

Models were refined using the MCSA method, in which atoms were allowed to displace from their crystallographic positions. Refinements were carried out over the range $3.1 < r < 10$ Å. This range is broad enough to make the refinement meaningful. However, it ignores the peaks in the function at low r that come from nearest-neighbor correlations. These peaks are considered in isolation and not included in the refinement.

Initially it was established that no static displacive disorder was associated with the copper or M sublattices. These ions were randomly displaced and the model refined. A global thermal parameter was also refined. In each case these ions refined to negligibly small displacement magnitudes. The largest refined displacement was for copper displacing parallel to z and this was 0.01 Å. This is smaller than the thermal broadening of peaks and cannot be considered to be significant. There is no displacive disorder associated with the M or Cu sublattices in agreement with the thermal factor evidence. In subsequent refinements, these ions were confined to their crystallographic positions.

Using this fact, a reliable value for a global thermal parameter could be established without including it as a variable parameter in subsequent refinements. The well-separated peak in the PDF at 3.3 Å originates from a Cu—M correlation. The breadth of this peak must be due to zero-point and thermal motion of the ions. Thus, the temperature factor for the sample was fixed at U_{ii}=12.5 pm^2, to fit this peak, and the only refinable parameters included in subsequent models were atom displacements. No more than five variables were used in any of the refinements that will be described.

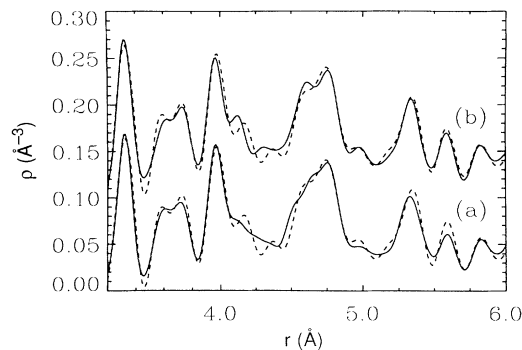Displacements were then introduced on oxygen sites.

FIG. 7. (a) Solid line: PDF of the best refined single-domain model. The oxygen displacements were uncorrelated from site to site. Dashed line: data PDF from the $x = 0.165$, 10 K, data. (b) Solid line: PDF of the best refined two-domain model. This is a mixture of the 2×2 model described in the text, with undistorted T' crystal, in the ratio 60:40. Dashed line: the same data as in (a). The PDF's in (b) are offset by 100 nm^{-3}.

Both O1 and O2 ions were allowed to displace parallel to the **a**, **b**, and **c** axes. The O1 and O2 ions were refined separately. Initially the displacements that were refined were uncorrelated from site to site. This is equivalent to there being a multiwelled potential at each O site with all the wells being equally populated on average. Only small values were refined for the displacement of O1 parallel to the Cu—O1 bond and these led to a minimal reduction in χ^2.[41] There is no good evidence that O1 is displaced parallel to the Cu—O1 bond. This displacement was fixed at zero in subsequent refinements. On the other hand, displacements of both O1 and O2 in all the other directions gave significant improvements in the agreement. When displacements in all these directions were introduced, χ^2 was reduced from 26.4 to 7.4, for a total of four refinable variables. The refined values for uncorrelated displacements are given in Table III and the resulting model PDF is shown in Fig. 7(a) superimposed over the data PDF.

It is clear from the refinements of thermal factors, and uncorrelated atom displacements, that significant displacements of oxygen ions are present in the structure.

1. Ordered oxygen displacements

It is more likely that, rather than being random from site to site, the oxygen displacements form some locally ordered superstructure with lower symmetry than the T' structure. The best evidence for this in the PDF comes from the nearest-neighbor atom pair correlations at small values of r. These peaks were not included in the refinements since they have the largest statistical and systematic errors associated with them and it was desired not to bias the refinements. However, introducing random displacements of oxygen on every site produced a broadening of these which was qualitatively too great. The implication is that displacements of nearest neighbors are correlated and atomic displacements are locally

ordered. A great many models were tried in which differently ordered "displacement structures" were refined. In these models similar oxygen displacements were introduced as in the uncorrelated models; however, a specific local ordering arrangement of the displacements was imposed. The CuO_4 plaquettes were allowed to tilt about axes parallel to $\langle 100 \rangle_{T'}$ or $\langle 110 \rangle_{T'}$, by displacing O1 systematically up and down parallel to c ($\Delta O1_z$), giving rise to a buckling of the plane. These tilts were combined with various displacement patterns for the O1 displacements in the plane ($\Delta O1_{xy}$) and combined with various cooperative displacements of O2 atoms ($\Delta O2_{xy}$, $\Delta O2_z$). None of these models emerged as being uniquely better than any other and none gave a significant improvement over the model with randomly displaced oxygen ions.

Important features of the PDF were not being well explained by any model of fixed amplitude displacements. In particular, there is a sharp peak in all the low-temperature ($T < 30$ K) data PDF's situated at 4.4 Å, which can be seen in the dashed line of Fig. 8 labeled C. This feature is particularly interesting because it exhibited a distinct temperature dependence which was associated with the appearance of superconductivity.[12] It is clear in the figure that in the low-temperature data (dashed line) this peak is much sharper than in the high-temperature data (dotted line). In both cases it is shifted with respect to the undistorted T' model PDF (solid line). This peak originates from a Cu—O1 second NN correlation. The challenge of the modeling became to explain how this peak could be asymmetrically shifted yet still be sharp. Without lowering the symmetry, atom displacements would symmetrically broaden the peak. It required a model in the 2×2 cell adequately to explain this feature while being consistent over the remainder of the PDF.

Features such as the one at 4.4 Å require the presence of relatively large, locally ordered displacements. However, the lowest χ^2 values were obtained when much smaller magnitude displacements were refined. Indeed better agreement was obtained from the model with uncorrelated displacements; however, in this model PDF
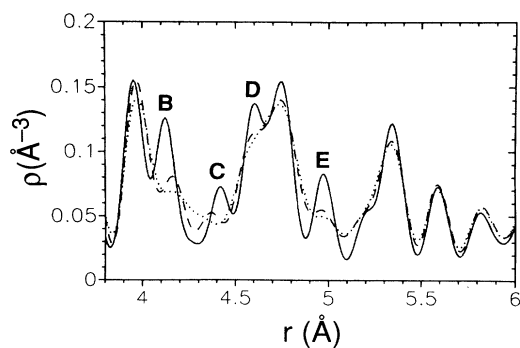
the peak at 4.4 Å was broadened out of existence. This can be seen clearly in Fig. 7(a) which shows this refined model PDF superimposed over the data PDF. These observations could be reconciled if the structure of the CuO_2 plane was locally inhomogeneous. In this picture, regions of the plane have ordered oxygen displacements with large magnitudes while other regions are relatively undistorted. The PDF is a superposition of all of the local regions of the crystal and features in the PDF will reflect the locally ordered displacements but will be broadened by the distribution of local environments.

This two domain hypothesis was tested by mixing together models of two end-member structures in varying proportions. One model was the T' model in which the CuO_2 planes are completely flat. Various models were used for the domains of highly displaced local structure. The one which was most successful was in the 2×2 cell and is described below. The ordered oxygen displacements are shown schematically in Fig. 9. In-plane displacements of $\Delta O1_{xy}$ are such as to distort the CuO_4 plaquettes from square to rectangular by systematically displacing O1 ions perpendicular to the Cu—O bond. Out of plane displacements of O1 are such as to tilt the plaquettes. In each case the tilt axis is parallel to the short edge of the plaquettes. Similar, accommodating displacements of $\Delta O2_z$ are also present. Two kinds of O2 sites can be differentiated. Those in which the $\Delta O1_z$ displacements on adjacent planes are in-phase (IP), and those in which they are out-of-phase (OP). $\Delta O2_z$ displacements on each of these sites were refined independently. Best results were obtained when some randomness was introduced in the $\Delta O2_{xy}$ displacements and so disordered $\Delta O2_{xy}$ displacements were used in this model.

Initially, this 2×2 model was not refined but displacement magnitudes were fixed at 0.1 Å. The PDF's of the 2×2 and the T' models were then mixed in varying proportions. The best agreement ($\chi^2 = 5.3$ for the range
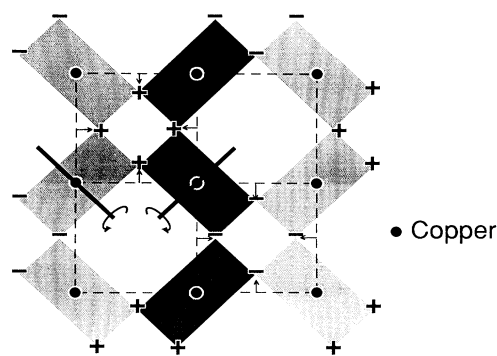

FIG. 8. Data PDF's from the $x = 0.165$ sample: 50 K (dotted line) and 10 K (dashed line) data, indicating the temperature dependence through T_c. The solid line is the model PDF from the undistorted T' structure. The peaks are labeled so as to be consistent with Fig. 6.

FIG. 9. Plain view of the CuO_2 plane indicating the pattern of oxygen displacements used in the 2×2 model. The shaded rectangles are the CuO_4 plaquettes; the darkness of the shading differentiates the sense of the tilt. Arrows indicate the in-plane ($\Delta O1_{xy}$) displacements and the plusses and minuses indicate the out-of-plane displacements ($\Delta O1_z$) of the O1 ion. Two of the plaquette tilt axes are shown as bars. The in-plane displacements are magnified for clarity.

$3.2 < r < 6.0$ Å) was obtained for the 2×2:T' ratio of 60:40. It is significant that neither of the end-member structures produces a good fit to the data ($\chi^2 = 25.3$ and 16.4 for the T' and large displacement 2×2 model respectively). However, the inadequacies of each model balance out those of the other, over the entire range of PDF considered, when they are mixed and a deep minimum in χ^2 is obtained as a function of mixing fraction. In this region there are ~ 20 inequivalent atom pair correlations contributing intensity to the PDF, yet the intensity distribution in the data could be accounted for self-consistently, with no fitting parameters, by the two models. This large deviation from perfect mixing behavior gives a strong indication that the mixture is real. This behavior is illustrated in Fig. 10. In this figure the end-member displaced structure used was refined from this 2×2 model as will be described, although it was fixed and not refined in the various mixtures. The figure is qualitatively the same as for the unrefined model described above except the minimum in χ^2 is reduced from 5.3 to 4.8 in this case. The best χ^2 value of the (unrefined) mixture model is comparable to the best refined models yet it produces a qualitatively much better fit on the important features at 4.2 Å and 4.4 Å. The qualitative fit to these features was not obtained in any model tried in the smaller T' or root-2 unit cells.

This two-domain mixture model was then refined over the range $3.2 < r < 6.0$ Å. The ratio of distorted to undistorted crystal was fixed at 60:40 and the undistorted T' model was not refined. Oxygen displacements were refined in the 2×2 model. These were constrained to reproduce the local ordering pattern described above leading to five refinable variables. The refined model PDF is shown in Fig. 7(b) superimposed over the data. χ^2 over the range of the figure was $\chi^2 = 4.8$ compared to $\chi^2 = 5.3$ for the single phase randomly displaced model shown in (a) of this figure. This can be seen in Fig. 10 in
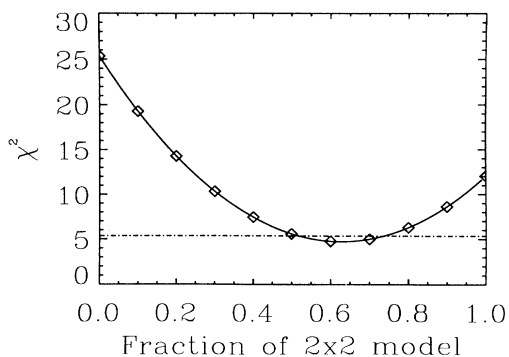

FIG. 10. Agreement between various models and the $x = 0.165$, 10 K data, calculated over the range of the PDF $3.2 < r < 6.0$ Å. Diamonds: χ^2 for models which are mixtures of heavily distorted crystal with undistorted crystal. The heavily distorted regions have the refined 2×2 local structure model described in the text. Notice the large negative deviation from normal mixing behavior. The dot-dashed line indicates the χ^2 value for the best single phase model.

which the diamonds show the χ^2 values for various mixtures of the undistorted T' structure with the refined 2×2 model just described. The dot-dashed line illustrates the χ^2 value of the refined single phase model with uncorrelated oxygen displacements. The mixture model gives a small improvement in χ^2 over the best single domain model; Furthermore, it reproduces the sharpness of the features in the data PDF at 4.2 Å and 4.4 Å.

It should be noted that the improvement in fit in the 2×2 cell is not because a larger cell allows more degrees of freedom. The constraints placed on the displacements by the ordering patterns mean that, whichever cell is considered, a maximum of five independent variables are allowed. Any improvement in agreement implies that the pattern of local displacements in the model gave a better description of the structure. An interesting outcome of the refinements was that it became clear that a distribution of O1—O2 bond lengths was preferred, to go along with the distributions of O1—O1 and O2—O2 bond lengths inherent in the model. In particular, it can be seen from Table III that the $\Delta O2_z$ displacements that were refined on IP sites refined to a small value. They did not refine a cooperative displacement with the neighboring $\Delta O1_z$ displacements which might have been expected from steric arguments. In fact, in some of the models tried in the 2×2 cell, a value for $\Delta O2_z$ was refined which was opposite in sign to the neighboring $\Delta O1_z$ displacements, even though the initial value for $\Delta O2_z$ was in-phase with these $\Delta O1_z$ displacements. This is strong evidence that a distribution of O1—O2 bond lengths is present in the highly distorted domains.

It would be of great interest to understand in more detail how the observed distortions affect the electronic structure of the material. Band calculations based on the long-range crystal structure of these materials do not take into account the significant differences in the local bonding and symmetry which are evident in the local atomic structure. To facilitate investigations into the properties of the displaced ion structures, we present atom coordinates for a displaced ion model. This model captures the essential features of the local structure within the distorted regions of crystal. The displacements of O1 used are those refined in the 2×2 model already described. For simplicity, we have removed all displacements of O2. These undoubtedly exist in the real material but appear to be disordered and even without these displacements the important features of the local structure are retained. These are the distribution of O1—O1 and O1—O2 bond lengths, and the lowered local symmetry in the plane. The atom coordinates are given in Table IV based on a unit cell in the $Cmc2_1$ space group. Although the symmetry is orthorhombic, there is no orthorhombic strain and $a = b = 11.175$ Å, $c = 12.100$ Å. This model will reproduce the local structure within the heavily distorted domains of the crystal. However, it should be noted that this is not the long-range crystal structure of $Nd_{2-x}Ce_xCuO_{4-y}$ since these domains are not ordered over long range.

In summary, the data PDF of $Nd_{2-x}Ce_xCuO_{4-y}$ at low temperature has only been satisfactorily explained when the symmetry is lowered by a local collective tilting

TABLE III. Displacement magnitudes Δ for the models described in the text. The uncorrelated displacements were refined with four independent variables. The 2×2 model was mixed in the ratio 60:40 with the undisplaced model and was refined with five variables. The χ^2 values were calculated over the range $3.1 < r < 10.0$ Å.

	χ^2	$\Delta O1_{xy}$[a] (Å)	$\Delta O1_z$ (Å)	$\Delta O2_{xy}$[b] (Å)	$\Delta O2_z$ (Å)
T'	26.4	0	0	0	0
Uncorrelated	7.4	±0.06	±0.07	±0.08	±0.06
2×2	7.1[c]	±0.10	±0.08	±0.10	$\pm0.01/0.06$[d]

[a]In directions perpendicular to the Cu—O1 bond only.
[b]In {110} directions.
[c]When mixed with undistorted T' in the ratio 60:40.
[d]The first value was the magnitude refined on IP sites and the second value was refined on OP sites. See text for details.

and straining of the CuO_4 plaquettes. These displacements are not ordered over long range and the CuO_2 plane is not homogeneous, but varies from being heavily buckled to being flat.

2. Estimate of domain size

It is desirable to know the size of the domains of distorted crystal. Information on the correlation length r_ξ of the local order is contained in the PDF. In the range $r < r_\xi$, atom pair correlations are predominantly intradomain. The total PDF thus appears as an incoherent superposition of the local order of both the distorted and undistorted domains. The best explanation of the data will be obtained from a two-domain mixture model. In the region $r \gtrsim r_\xi$, most of the atom pair correlations will be interdomain. In this case the data will be best explained by a single phase model which contains some displacive disorder: atom displacements will be evident but the local order of the displacements is lost. Finally, for large values of r, the long-range order of the crystal will dominate and the crystallographic model should begin to give the best explanation of the data. Thus, by considering the relative performance of three models as a function of r in the PDF, we can learn about the magnitude of r_ξ. In particular, we will compare the χ^2 values from the two-domain mixture model (M), the best refined single phase model which has uncorrelated oxygen displacements (R), and the crystallographic T' model (T). The results are summarized in Figs. 10 and 11. Figure 10 contains the χ^2 values for the models in the region $3.2 < r < 6.0$ Å (region I). The two-domain model values are plotted as diamonds. The dot-dashed line is the χ^2 value for the R model. The χ^2 value for the T model is given by the point of the two-domain model for zero fraction. The data are presented in similar fashion in Fig. 11. In this figure, the diamonds and the dot-dashed line refer to the region $6.0 < r < 12.0$ Å (region II) and the triangles and the dash-dotted-dotted-dotted line refer to the region $12.0 < r < 20.0$ Å (region III). In region I the M model has a slightly better χ^2 value. This two-domain model also gives the best description of the PDF, as we have discussed. It exhibits a remarkable

negative deviation from perfect mixing, as indicated by the deep minimum in the curve of Fig. 10, and provides the best qualitative description of the PDF in this region. In region II the R model appears to do better than the mixture model. The minimum in the curve of the mixture model is less pronounced and the R model has a lower χ^2 value than the best mixture model. In region III the models have a remarkable reverse of fortunes. In the region above 12.0 Å the crystallographic model gives a much better agreement than any model which includes atom displacements. It should be noted that this effect may, in part, be due to an experimental artefact. The r-dependent contribution to the PDF peak broadening (see Sec. IV B) may overestimate the broadness of peaks in the high-r region. The effect is only significant for $r > 10$ Å,[23] where it will tend to bias the agreement in

TABLE IV. Atom coordinates for the refined 2×2 model described in the text. This structure is not ordered over long range in $Nd_{2-x}Ce_xCuO_{4-y}$. It represents a model for the local structure within the heavily distorted regions of the crystal. However, for convenience, it is presented as atom coordinates in a unit cell. The model is in the orthorhombic space group $Cmc2_1$ with $a = b = 11.175$ Å and $c = 12.100$ Å.

| Site	x	y	z
Nd/Ce	0.2500	0.1250	0.1475
Nd/Ce	0.0000	0.3750	0.1475
Nd/Ce	0.5000	0.3750	0.1475
Nd/Ce	0.0000	0.1250	0.3525
Nd/Ce	0.5000	0.1250	0.3525
Nd/Ce	0.2500	0.3750	0.3525
Cu	0.0000	0.1250	0.0000
Cu	0.5000	0.1250	0.0000
Cu	0.2500	0.3750	0.0000
O1	0.1187	0.9937	0.0066
O1	0.3813	0.9937	0.9934
O1	0.1187	0.2563	0.9934
O1	0.3813	0.2563	0.0066
O2	0.1250	0.0000	0.2500
O2	0.3750	0.0000	0.2500
O2	0.1250	0.2500	0.2500
O2	0.3750	0.2500	0.2500
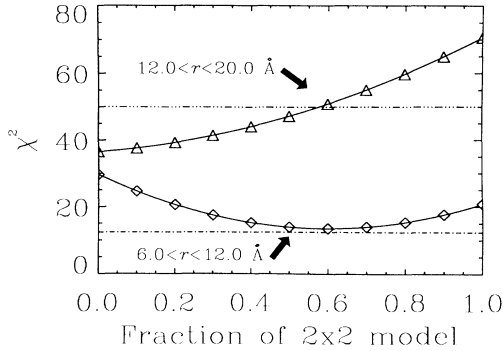
FIG. 11. Similar plots to those shown in Fig. 10; however, in this case the χ^2 values were calculated over the ranges of the PDF: $6.0 < r < 12.0$ Å (diamonds and dot-dashed line), and $12.0 < r < 20.0$ Å (triangles and dash-dotted-dotted-dotted line).

favor of an undistorted model over one with distortions. In region II the effect should be small but would tend to raise the χ^2 value of the R model with respect to the M model. In fact, even with this effect, χ^2 for the R model is lower than the best M model.

We can conclude from these observations that, already by region II, a significant proportion of the atom pair correlations are interdomain and the domain size is of the order of 6 Å. This would also explain why the R model can get a comparable agreement even in region I. With such small domains, even though intradomain correlations dominate in region I, there will also be a significant contribution to the PDF from interdomain correlations. However, we reiterate that the single domain model alone cannot explain the lowered local symmetry evident in the PDF in region I.

VI. DISCUSSION

A. Occurrence of CuO_2 plane distortions

The presence, and detailed structure, of tilts of CuO_6 octahedra have a profound effect on the properties of the $La_{2-x}(Sr,Ba)_xCuO_4$ materials, as evidenced by the behavior of the LTT phase. It is thus of great interest to observe similar structural distortions in the n-type superconductor $Nd_{2-x}Ce_xCuO_{4-y}$. It is the more interesting since they are not expected based on simple steric arguments. It is widely thought[42] that the CuO_6 tilts in $La_{2-x}(Sr,Ba)_xCuO_4$ are driven by inherent size incompatibilities in the structure. We will discuss this hypothesis, but argue that this picture is too simple and cannot explain all the experimental observations.

$La_{2-x}Ba_xCuO_4$ can be made superconducting in the approximate range of doping $0.08 \lesssim x \lesssim 0.2$.[43] However, over a very narrow range of doping, close to $x = \frac{1}{8}$, a dramatic drop in T_c is observed with a concomitant decrease in the Meissner fraction of the sample. This behavior coincides with the appearance of the LTT structure.[4] The crystal structure of $La_{2-x}Ba_xCuO_4$ is based on the tetragonal K_2NiF_4 structure.[44] This has single CuO_2

planes separated by intergrowth regions of composition LaO which have the NaCl structure. The copper ions in the plane exist at the center of distorted octahedra of oxygen ions. At low temperature they become collectively tilted.[45]

The CuO_2 plane and the NaCl intergrowth region, in isolation, have their own ideal lattice parameters which depend on the natural Cu—O and La—O bond lengths respectively. A mismatch parameter m can be defined which is a measure of the compatibility of these two regions of the lattice,

$$m = \frac{\sqrt{2}(r_{Cu^{2+}} + r_{O^{2-}})}{r_M + r_{O^{2-}}} - 1 \qquad (14)$$

where the r_A's are ionic radii, which can be obtained, for instance, from the tables of Shannon and Prewitt,[39] and M denotes an alkaline-earth or rare-earth ion. The value of m is small and positive ($m = 0.09$) in La_2CuO_4. The value of m can change as a function of doping, i.e., the substitution of larger Ba^{2+} or Sr^{2+} ions for La^{3+} ions. It can also change as a function of temperature because of different thermal expansivities for the two crystal regions.[42] The real crystal is continuous, and the true mismatch is constrained to be ~ 0. This implies that in the real structure the CuO_2 plane experiences a compressive stress. This fact seems to explain a number of apparent features of the $La_{2-x}(Ba,Sr)_xCuO_4$ phase diagram and its properties. These materials are hole doped. Local-density approximation (LDA) calculations indicate that the band that is most likely to accept doped carriers is the broad band of Cu $d_{x^2-y^2}$, O p_{xy} character. This band is a half-filled σ^* antibonding band which is split into upper and lower Hubbard bands by the correlation energy U. Since it is an antibonding band, doping holes into this band will tend to stabilize the Cu—O1 bond, lower m, and thus relieve the compressive stress. Doping electrons will have the opposite effect. Indeed it has proved impossible to dope electrons into materials with the La_2CuO_4 structure. Another way to relieve the compressive stress on the planes is for them to buckle. This type of oxygen bond bending distortion is well known in ferroelectric perovskite materials such as $SrTiO_3$ (Ref. 46) where it is driven by a ferroelectric instability. Again, this behavior is observed in $La_{2-x}(Sr,Ba)_xCuO_4$. According to the long-range crystal structure, the planes are flat at high temperature. On cooling, these materials undergo the second-order high-temperature tetragonal (HTT) to low temperature orthorhombic (LTO) structure transition[47] which includes a buckling of the CuO_2 plane by collective CuO_6 tilting. A different situation prevails in the T' structure of $Nd_{2-x}Ce_xCuO_{4-y}$. In this case the mismatch parameter $m' < 0$ and the CuO_2 plane experiences a tensile stress due to the intergrowth layer. By similar arguments one would expect the CuO_2 plane to be flat and the materials to prefer n-type doping. Indeed the T' phase has never successfully been doped with holes and $Nd_{2-x}Ce_xCuO_{4-y}$ does not undergo a phase transition into a lower symmetry plane-buckled state.

The mismatch model for the driving force for the distortions is consistent with observed long-range structure

and doping phenomena in the 2:1:4 materials. However, our observation is that locally there *is* significant buckling of the plane in $Nd_{2-x}Ce_xCuO_{4-y}$ and this cannot be explained by lattice mismatch arguments. It is also not clear, within this picture, why doping the relatively larger Ba^{2+} and Sr^{2+} ions for smaller La^{3+} ions in $La_{2-x}(Ba,Sr)_xCuO_{4+y}$ tends to stabilize the HTT phase.[48] Finally, it has also been observed from the PDF that the CuO_2 planes in the infinite layered insulator $Ca_{0.85}Sr_{0.15}CuO_2$ are not flat, but are also buckled;[31] in this case the CuO_2 layers are separated simply by calcium and strontium ions. It is clear that the simple steric arguments presented above cannot explain all of the experimental observations. There must be an additional driving force producing these plane-buckling distortions.

B. Local order of distortions

Before proceeding, it is interesting to examine our best model in more detail. This model was preferred for the reasons given in Sec. V C 1, although alternative descriptions of the fine details of the local structure cannot be ruled out. It envisages the plane to be inhomogeneous with a distribution of more or less heavily displaced domains which are continuously distributed throughout the plane. In the buckled regions a very distinct local symmetry is observed and the displacements are highly correlated. On a local level, the symmetry is reduced from the crystallographic symmetry. In the distorted regions the symmetry is orthorhombic and there is no inversion symmetry. This may explain recent Raman scattering and infrared absorption results on $Nd_{2-x}Ce_xCuO_{4-y}$ materials.[49] In this study several well-defined vibrational peaks were observed which appeared to be intrinsic to materials in this system but which could not be explained using the undistorted T' structure. For example, a resonantly enhanced peak was observed in the Raman spectrum at 580 cm^{-1} in Ce-doped samples. This mode has A_{1g} symmetry and does not correspond to any Raman allowed regular phonon modes. It is a clear indication that the atomic structure of these materials is distorted from the T' structure. The energy and symmetry of the mode suggest an oxygen stretching mode parallel to c. In our 2×2 model there are a distribution of O1—O2 bond lengths. The local symmetry is lower than the T' structure and is noncentrosymmetric. It is possible that this Raman feature is caused by local modes which are associated with the heavily distorted regions of crystal.

The nature of the proposed local order of the displaced ions is also interesting in itself. First, we observe that it was necessary to introduce displacements of O1 both parallel and perpendicular to the plane. The perpendicular displacements give rise to the plane buckling. In the 2×2 model, the in-plane displacements strain the CuO_4 plaquette, in direct analogy with the orthorhombic strain observed in the LTO phase of $La_{2-x}(Sr,Ba)_xCuO_4$.[45] The square plaquettes become rectangular, although to first order the Cu—O1 bond is not changing length; rather

the O1—O1 bonds are becoming respectively long (l) and short (s). A plaquette strain can be defined as

$$\epsilon_p = \frac{l - s}{(l + s)/2}. \tag{15}$$

For displacements of $\Delta O1_{xy} = \pm 0.1$ Å, $\epsilon_p = 0.098$. This is an order of magnitude larger than the long-range orthorhombic strain observed in the LTO structure. The possibility exists that on the local scale the orthorhombic distortion of the octahedra in $La_{2-x}(Sr,Ba)_xCuO_4$ is much larger than the observed macroscopic strain but the strained octahedra are not perfectly ordered over long range. It should also be noted that early PDF experiments on $La_{1.85}Sr_{0.15}CuO_4$ indicated that, even in the HTT phase, the CuO_2 planes were not flat, but appeared to be buckled.[50] The HTT to LTO transition is probably an order-disorder, rather than a distortive, transition.

It is also interesting that the best 2×2 model has all tilts of the CuO_4 plaquettes about axes parallel to the short edge of the plaquette. Again, this behavior is in direct analogy with the LTO structure, although in the present case the plaquettes are not lined up in space and there is no long-range orthorhombic strain.

In successive CuO_2 planes the Cu ion is displaced by $[\frac{1}{4}\frac{1}{4}\frac{1}{2}]$ with respect to the 2×2 unit cell. This means that the proposed pattern of tilts of the CuO_4 plaquettes is not compatible from one plane to the next. As we discussed in Sec. V, each O2 ion is shared equally between adjacent CuO_2 planes. Thus, because of the incompatibility between the oxygen displacement structure of each plane, $\Delta O2_z$ displacements cannot be simultaneously correlated with $\Delta O1_z$ displacements in both adjoining planes. Consequently, some disorder should be associated with the $\Delta O2$ displacements due to this frustration. This was observed in PDF refinements which refined a distribution of O1—O2 bond lengths.

In this model the local symmetry *within* the planes dominates over the interplanar order. To check whether this was indeed the case, an alternative model was tried where the opposite was true. A different pattern of ΔO_z displacements was tried in which all ΔO_z displacements were continuous from one plane to the next. In this model the O1—O2 rods displaced rigidly. This model was less successful than models which could refine a distribution of O1—O2 bond lengths. It appears that the driving force for the displacements preserves their local order *within* the plane without requiring coherence between the planes. The mechanism that stabilizes these distortions should be able to explain the distinct local symmetry and the preeminence of the intraplane order.

Finally, we make one further observation about the oxygen displacements. It is not known if the oxygen displacements are static or dynamic; however, it is probable that they are dynamic. We observed that features in the PDF were somewhat sensitive to the angle of the detector banks. As discussed in Sec. III B, this is indicative of a dynamic origin of those features. As we will discuss, the observed change in the PDF associated with T_c (Ref. 12) can be explained by a change in the lattice dynamics close to the superconducting transition.

C. Driving force distortions

In this section we will argue that the observed lattice distortions could be a direct observation of large, mobile, polarons or bipolarons. However, the polaronic states cannot originate from the impurity doped electrons, nor from the Cu—O σ^* band. We envisage that they originate from certain narrow O p bands. The implications of this picture are that there exist two electronic subsystems on the CuO_2 plane. Highly mobile impurity doped electrons in the C—O σ^* band coexist with polaronic lattice induced hole states. The polaronic states are mobile and are likely to be critical for the superconducting property.

Our experimental observation is that significant displacements of oxygen are present in the material giving rise to tilted and strained CuO_4 plaquettes. The magnitude and extent of these displacements is too large to be explained solely by the presence of defects in the lattice. They appear to be intrinsic to the structure. This is further borne out by the fact that similar distortions have been observed in related materials such as $Tl_2Ba_2CaCu_2O_8$ and $Ca_{1.85}Sr_{0.15}CuO_2$.[11,31] However, one might expect that an intrinsic lattice instability would order over long range at some temperature, giving rise to a phase transition. This is not observed in $Nd_{2-x}Ce_xCuO_{4-y}$. The distortion remains local and the atom displacements are inhomogeneous even at low temperature. It thus appears that this inhomogeneity is also an intrinsic property of the structure. The formation of, localized, self trapped polaronic carriers in these structures would give a very natural explanation of this behavior.

The observed atom displacements affect to first order O—O bond lengths. In the undistorted crystal $r_{(O1-O1,O2-O2)} = 2.79$ Å, and $r_{O1-O2} = 3.02$ Å. After introducing oxygen displacements there are a range of values for these two bond lengths. These are $2.65 < r_{(O1-O1,O2-O2)} < 2.93$ Å and $2.82 < r_{O1-O2} < 3.22$ Å, where these values should be considered as upper bounds. The electronic states that will be most affected by this distribution of bond lengths are those in the O1 p_{xy}–O1 p_{xy}, O2 p_{xy}–O2 p_{xy}, and O1 p_z–O2 p_z bands. LDA band calculations[51] indicate that these states form narrow bands which lie just below the Fermi surface in the undistorted material. The possibility exists that the lattice distortion could raise the energy of certain O p states through the Fermi surface. A simple calculation can be carried out to estimate the magnitude of this change in energy. We take the form for the atomic orbital overlap energy due to Harrison.[52] The form is reminiscent of the change in energy of a free-electron metal with changing lattice parameter. However, it has also been shown to give very good empirical agreement with the behavior of various covalent solids.[52] It should be adequate for making an estimate of the magnitude of the change in energy of O p band states due to the lattice distortion. For overlap of oxygen p states, giving rise to a σ bond, the overlap energy is given by

$$V_{pp\sigma} = \eta_{pp\sigma} \left(\frac{\hbar^2}{md^2} \right), \tag{16}$$

where $\eta_{pp\sigma}$ is a dimensionless geometrical factor, m is the bare electron mass, and d is the separation of the neighboring atoms. We can define the change in overlap energy due to the oxygen displacements as $\Delta V_{pp\sigma} = V_{pp\sigma}(d_1) - V_{pp\sigma}(d_0)$, where d_1 is the shortest oxygen-oxygen bond length after displacement and d_0 is the length of the same bond undistorted. Using the value for $\eta_{pp\sigma}$ due to Louie[53] of 2.22 we get that $\Delta V_{pp\sigma} = 0.24$ eV for in-plane interactions and $\Delta V_{pp\sigma} = 0.27$ eV for out-of-plane interactions. In LDA band calculations[51] the O p bands come within 0.2 eV of the Fermi level. Thus, it appears that the observed distortions are consistent with the idea that regions of the O p bands could be raised through the Fermi level. This would introduce holes into the affected bands which would remove electron density from the unfavorable regions of the lattice between squeezed O^{2-} ion pairs. There will be an energy saving associated with this. If this energy saving is greater than the cost in elastic energy of distorting the lattice then the lattice distortion will be stabilized by a self-trapped hole, or polaron. Emin[54] has shown that the dielectric properties of HTSC's materials are favorable for polaron formation. It is also known that carrier localization is easier in narrow bands,[55] and that the presence of a correlation energy U and antiferromagnetic interactions can also help the carrier localization process.[56,57]

The existence of polaronic states in these materials is a real possibility. It is thus interesting to understand how polarons would appear in the PDF. Polarons can be split into two broad classes: small polarons and large polarons.[54] A small polaron exists when the carrier collapses onto a single atomic site. It is stabilized by large displacements of nearest-neighbor ions and has the appearance of a point defect in the structure. These polarons are highly immobile. For the carrier to hop the neighbor ions must move through a distance many times their quantum zero-point amplitude. A large polaron is spread out over many atom sites and can have a radius up to a few tens of angstroms. They are characterized by a large number of atoms having a relatively small displacement. The ground state of the polaron will be associated with a particular ordering arrangement of the atomic displacements associated with it. The polarons must be spatially separated by undistorted regions of lattice. From this it appears that the observed distortion in $Nd_{2-x}Ce_xCuO_{4-y}$ is consistent with the observation of large polarons. From the PDF we see that the oxygen displacements are correlated over a range of at least 6 Å in the CuO_2 plane with a definite local symmetry. However, the plane is not homogenous and exhibits regions of distorted and undistorted crystal which are necessary for polarons not to overlap.

Large polarons are mobile.[54] For a self-trapped carrier to move it must be accompanied by its local lattice distortion. Thus, we would expect that mobile bipolarons would have a distinct effect on the lattice dynamics of the local structure. The PDF experiment does not yield direct information about lattice dynamics, but as discussed in Sec. II, it is sensitive to them. If a dynamic excitation, such as a moving bipolaron, exists, it will have one of three effects on the PDF. If it is very slow it will appear

in the total $S(Q)$ but will not be significantly distorted by the inadequate energy integration. The dynamic feature will appear as a sharp feature in the PDF preserving the structural information it contains. At intermediate energies the excitation will appear in the measured $S(Q)$ but it will be broadened significantly by the inadequate energy integration. The resulting features in the PDF will be broad and will become very indistinct. The final possibility is that the excitation has such a high energy that it falls outside the energy bandwidth of the experiment. In this case it will not appear in the total $S(Q)$ at all and the excitation will not be evident in the PDF. The PDF will represent the "time-averaged" structure with respect to that dynamic feature.

The PDF of $Nd_{1.835}Ce_{0.165}CuO_{4-y}$ exhibits a change as the material goes superconducting.[12] This change is illustrated in Fig. 8. Above T_c the features at 4.2 Å and 4.4 Å are very broad. Just above T_c they begin to sharpen up and the highest points of the features shift.[12] Finally, below T_c the features stabilize in the positions that they appear in the 10-K data (dashed line) in Fig. 8. This kind of behavior might be expected of bipolarons, which are moving moderately quickly above T_c, begin to slow down in the critical region just above T_c, and finally condense below T_c. Thus, the observation in the PDF of features shifting and becoming sharper as the sample goes superconducting could be explained as the direct observation of large, mobile, bipolarons which are involved in the superconductivity of the material.

D. Mechanism for superconductivity

Rather than propose a detailed mechanism for superconductivity in $Nd_{2-x}Ce_xCuO_4$ we will simply present a general justification for the assertion that we may be observing bipolarons in the PDF.

It is not possible to determine directly from the PDF whether lattice distortions are polaronic, bipolaronic, or have some other origin. We have argued that the data PDF is consistent with the presence of large polarons or bipolarons in the structure. The conditions under which bipolarons are stabilized with respect to polarons are rather severe; however, Emin has argued that these conditions are met in the high-T_c materials.[54] Furthermore, recent calculations[58] indicate that, in certain regimes of carrier density, the actual ground state of a system of dilute, interacting, carriers in a fixed homogeneous background of opposite charge, is not the Wigner crystal[59] but a state where the carriers are paired. In this regime there is a tendency for the formation of bipolarons over polarons due to an intrinsic property of the electron (or hole) gas, in addition to any driving force such as a reduction in lattice elastic energy. Bipolarons are examples of negative-U centers.[60] It has long been recognized that real-space pairing through negative-U centers could give rise to superconductivity.[55] The obvious route to bipolaronic superconductivity is a direct bose-condensation of mobile bipolaronic pairs at T_c. Another possibility which is relevant in the current case is a two component mechanism where localized pair states and delocalized,

unbound, states coexist. The existence of superconductivity in such a system has been explored by a number of authors.[61,62] By allowing transitions between these two subsystems the carriers can enjoy the pairing provided by the bipolarons, and the mobility provided by the free carriers. This mixing produces a superconducting condition of the whole system, where neither of the subsystems alone would be superconducting. Such a mechanism has been proposed to explain the superconductivity in $Tl_2Ba_2CaCu_2O_8$.[14,63] In this material similar plane-buckling lattice distortions have been observed by the PDF technique.[11,63] In this case the lattice-induced hole states appear to originate from the Cu d_{z^2} O p_z states, where the oxygen involved is in the apical site. Such a mechanism would also be possible in $Nd_{2-x}Ce_xCuO_{4-y}$ if the observed structural distortions are lattice-induced p-type bipolarons which coexist with the impurity doped n-type carriers.

A crude calculation of the condensation temperature of the bipolarons can be made based on parameters obtained experimentally from the PDF. The bose-condensation temperature T_{bc} increases with increasing density n of bosons, and decreases with the effective mass m_b of the bosons:[64]

$$T_{bc} = \frac{2\pi\hbar}{m_b k_B} \left(\frac{n}{2.612} \right)^{\frac{2}{3}}, \qquad (17)$$

where k_B is the Boltzmann constant. As the bipolaron moves, the lattice must move with it and the effective mass of the bipolaron thus depends on the mass of the atoms that have to move, and on the magnitudes of the displacement they are forced to make. The effective mass of the polaron depends on the weighted sum of the contributions due to all of the ions involved in the bipolaron's motion[65]

$$m^* = \sum_i M_i \left(\frac{\Delta d_i}{a} \right)^2, \qquad (18)$$

where M_i are the ion masses and Δd_i are the displacements that they undergo to translate the bipolaron one lattice spacing, a. The sum is over all those ions which must respond to the shift of the charge. Using this equation we can estimate the effective mass of the observed bipolarons. We take a simple minded model of the polaron as being a disk of radius 6 Å. This is the smallest radius that is consistent with our observation of the domain-mixture structure in the PDF. Assume that inside this radius, oxygen ions are displaced by 0.1 Å, and outside the radius they are undisplaced. A plain view of the CuO_2 plane, exhibiting the polaron, is shown in Fig. 12. We can see that, on moving the polaron one lattice spacing, ten oxygen ions move either into or out of the polaron. These ions are shaded in the figure. Thus, using Eq. (18), we get $m^* \approx 200 m_e$, where m_e is the electron mass.

We can also estimate the bipolaron density. Assuming 6 Å radius polarons with a 50:50 filling ratio, the carrier density would be $\approx 0.06/Cu$. If the superconductivity is confined to a region 3 Å thick about the CuO_2 plane, the bipolaron density $n = 1.25 \times 10^{21}$ cm^{-3}. Substituting
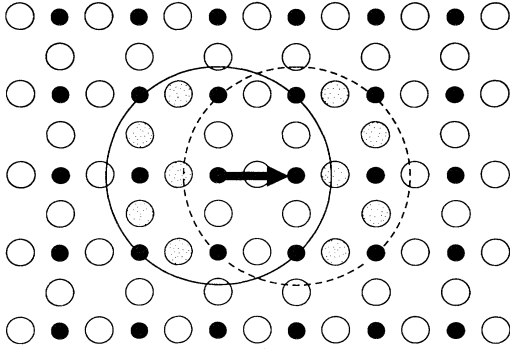
FIG. 12. Plain view of the CuO_2 plane indicating the presence of a moving polaron. The shaded atoms are the ones that would have to adjust their positions for the polaron to move one lattice spacing (Ref. 6.)

these values into Eq. (17), we get a predicted condensation temperature of ≈ 17 K, which is the correct order of magnitude. By this reasoning, the superconductivity in $Nd_{2-x}Ce_xCuO_{4-y}$ could be associated with a condensation of the bipolarons that are indicated in the PDF.

One argument against the existence of bipolaronic superconductivity in these materials has been that the observed carrier densities were much too high. At these carrier densities polarons that were large enough to be mobile and give the observed metallic behavior of HTSC's would severely overlap and the polaronic state could not survive. However, in our picture the polarons exist independently of the doped carriers. Presumably the normal state transport would be dominated by the impurity doped carriers but the superconductivity is a condensation of the minority carriers, or more likely, of both components of the electronic system; electrons and lattice induced holes.

This discussion was intended to assert that the appearance of oxygen displacements in the PDF may be the first direct observation of polarons or bipolarons in the structure of the high-T_c cuprates. A number of alternative theories also exist in which details of the local atomic structure are important for superconductivity.[66]

VII. CONCLUSIONS

The local structure of $Nd_{2-x}Ce_xCuO_4$ is significantly different from that implied by the periodic crystal structure. In particular, oxygen is locally displaced from its crystallographic position with a definite local symmetry. The CuO_4 plaquettes of the structure are strained and

tilted in a manner reminiscent of the LTO structure of $La_{2-x}(Sr,Ba)_xCuO_4$. However, these displacements are not ordered over long range and the CuO_2 plane is quite inhomogeneous with a distribution of undistorted and distorted domains. We have presented a model for this local structure and, from the PDF, estimate the size of the domains as ≈ 6 Å. Changes in the experimentally obtained PDF close to T_c, and observation of the diffraction angle dependence of certain features in the data, suggest that the displacements are dynamic. The behavior at T_c is reminiscent of a slowing down of the local structure fluctuations. The inhomogeneity of the plane and the dynamic nature of the displacements suggest an interpretation that they are mobile polarons. The nature of the displacements indicate that the polarons originate from O p states which lie very close to E_f in the undistorted structure. A slowing down of the polarons at T_c would indicate their involvement in the superconductivity, and that they are actually doubly occupied bipolarons. We argue that this picture is at least plausible based on an estimate of T_c using parameters taken from the experiment. Whether or not this is a direct observation of the existence of polarons, it is clear that the local atomic structure of HTSC's can be quite different from the long-range crystal structure. This should be taken into account when predicting the properties of these materials, for instance, using LDA calculations. The real-space refinement of the PDF has shown that it is a powerful technique for extracting local structural information.

ACKNOWLEDGMENTS

*Present address: Condensed Matter and Thermal Physics Group, Los Alamos National Laboratory, Los Alamos, NM 87545.

[1]R. J. Cava, A. W. Hewat, E. A. Hewat, B. Batlogg, M. Marezio, K. M. Rabe, J. J. Krajewski, W. F. Peck, Jr., and L. W. Rupp, Jr., Physica C **165**, 419 (1990).

[2]B. W. Veal, H. You, A. P. Paulikas, H. Shi, Y. Fang, and J. W. Downey, Phys. Rev. B **42**, 4770 (1990); H. Claus, S. Yang, A. P. Paulikas, J. W. Downey, and B. W. Veal, Physica C **171**, 205 (1990).

[3] J. D. Jorgensen, Shiyou Pei, P. Lightfoot, Hao Shi, A. P. Paulikas, and B. Veal, Physica C **167**, 571 (1990).

[4] J. D. Axe, A. H. Moudden, D. Holwein, D. E. Cox, K. M. Mohanty, A. R. Moodenbaugh, and Youwen Xu, Phys. Rev. Lett. **62**, 2751 (1989).

[5] M. K. Crawford, M. N. Kunchur, W. E. Farneth, E. M. McCarron III, and S. J. Poon, Phys. Rev. B **41**, 282 (1990).

[6] S. J. L. Billinge and T. Egami, in *Lattice Effects in High-T_c Superconductors*, edited by Y. Bar-Yam (World Scientific, Singapore, 1992).

[7] R. Zeyher and G. Zwicknagl, Solid State Commun. **66**, 617 (1988).

[8] M. Lang, R. Kürsch, A. Grauel, C. Geibel, F. Steglich, H. Reitschel, T. Wolf, Y. Hidaka, K. Kumagai, Y. Maeno, and T. Fujita, Phys. Rev. Lett. **69**, 482 (1992).

[9] S. D. Conradson and I. D. Raistrick, Science **243**, 1340 (1989).

[10] R. P. Sharma, L. E. Rehn, P. M. Baldo, and J. Z. Liu, Phys. Rev. B **40**, 11 396 (1989); L. E. Rehn, R. P. Sharma, P. M. Baldo, Y. C. Chang, and J. Z. Liu, *ibid.* **42**, 4175 (1990).

[11] B. H. Toby, T. Egami, J. D. Jorgensen, and M. A. Subramanian, Phys. Rev. Lett. **64**, 2414 (1990).

[12] S. J. L. Billinge, T. Egami, D. R. Richards, D. G. Hinks, B. Dabrowski, J. D. Jorgensen, and K. J. Volin, Physica C **179**, 279 (1991).

[13] S. J. L. Billinge, T. Egami, H. D. Rosenfeld, and T. Sendyka (unpublished).

[14] T. Egami, B. H. Toby, S. J. L. Billinge, Chr. Janot, J. D. Jorgensen, D. G. Hinks, M. K. Crawford, W. E. Farneth, and E. M. McCarron, in *High Temperature Superconductivity: Physical Properties, Microscopic Theory and Mechanisms*, edited by J. Ashkenazi *et al.* (Plenum, New York, 1992).

[15] M. Arai, K. Yamada, Y. Hidaka, S. Itoh, Z. A. Bowden, A. D. Taylor, and Y. Endoh, Phys. Rev. Lett. **69**, 359 (1992).

[16] See, for example, K. Suzuki, in *Neutron Scattering*, edited by K. Sköld and D. L. Price (Academic, New York, 1986), Pt. B; Y. Waseda, in *The Structure of Non-Crystalline Materials* (McGraw-Hill, New York, 1980).

[17] T. Egami, Mater. Trans. **31**, 163 (1990).

[18] B. E. Warren, *X-Ray Diffraction* (Dover, New York, 1990); S. W. Lovesey, *Theory of Neutron Scattering from Condensed Matter, Vol. 1* (Clarendon, Oxford, 1984).

[19] J. P. Hansen and I. R. McDonald, *Theory of Simple Liquids* (Academic, London, 1976).

[20] R. McQueeney and T. Egami (unpublished).

[21] J. D. Jorgensen, J. Faber, J. M. Carpenter, R. K. Crawford, J. R. Haumann, R. L. Hitterman, R. Lkeb, G. E. Ostrowski, R. J. Rotella, and T. G. Worlton, J. Appl. Crystallogr. **22**, 321 (1988).

[22] P. Lightfoot, D. R. Richards, B. Dabrowski, D. G. Hinks, S. Pei, D. T. Marx, A. W. Mitchell, Y. Zheng, and J. D. Jorgensen, Physica C **168**, 627 (1990).

[23] B. H. Toby and T. Egami, Acta. Crystallogr. Sect. A **48**, 336 (1992).

[24] D. L. Price (unpublished).

[25] S. J. L. Billinge, Ph.D thesis, University of Pennsylvania, 1992.

[26] I. A. Blech and B. L. Averbach, Phys. Rev. **137**, A1113 (1965).

[27] G. Placzek, Phys. Rev. **86**, 377 (1952).

[28] M. Misawa, D. L. Price, and K. Suzuki, J. Non-Cryst. Solids **37**, 85 (1980).

[29] W. C. Hamilton, *Statistics in Physical Science* (Ronald, New York, 1964).

[30] E. Prince, *Mathematical Techniques in Crystallography and Materials Science* (Springer-Verlag, New York, 1982); W. H. Press, B. P. Flannery, S. A. Teukolsky, and W. T. Vetterling, *Numerical Recipes* (Cambridge University Press, England, 1986).

[31] S. J. L. Billinge, P. K. Davies, T. Egami, and C. R. A. Catlow, Phys. Rev. B **43**, 10 340 (1990).

[32] See, for example, D. Chandler, *Introduction to Modern Statistical Mechanics* (Oxford University Press, England, 1987), pp. 159–183.

[33] B. H. Toby (unpublished) .

[34] Y. Tokura, H. Takagi, and S. Uchida, Nature **337**, 345 (1989).

[35] Hk. Müller-Buschbaum and M. Scheizer, Z. Anorg. Allg. Chem. **414**, 76 (1975).

[36] G. H. Kwei, S.-W. Cheong, Z. Fisk, F. H. Garzon, J. A. Goldstone, and J. D. Thompson, Phys. Rev. B **40**, 9370 (1989).

[37] F. Izumi, Y. Matsui, H. Takagi, S. Uchida, Y. Tokura, and H. Asano, Physica C **159**, 433 (1989).

[38] Compare this region of the PDF in Figs. 4 and 5, with the the shape of the data PDF.

[39] R. D. Shannon and C. T. Prewitt, Acta Crystallogr. **925**, 946 (1969).

[40] S. J. L. Billinge, C. R. A. Catlow, T. Egami, and Xiaozhong Zhang (unpublished).

[41] χ^2 was reduced from 26.4 for the undistorted T' model to 19.8 for the model with displacements of O1 parallel to the Cu—O1 bond.

[42] J. B. Goodenough and J. Zhou, Phys. Rev. B **42**, 4276 (1990); J. B. Goodenough, A. Manthiram, and J. Zhou, in *High Temperature Superconductors: Relationships Between Properties, Structure, and Solid-State Chemistry*, edited by J. D. Jorgensen, K. Kitazawa, J. M. Tarascon, M. S. Thompson, and J. B. Torrance, Mater. Res. Soc. Symp. Proc. No. 156 (Materials Research Society, Pittsburgh, 1989), p. 339.

[43] J. G. Bednorz and K. A. Müller, Z. Phys. B **64**, 189 (1986).

[44] J. D. Jorgensen, M. A. Beno, D. G. Hinks, L. Soderholm, K. J. Volin, R. L. Hitterman, J. D. Grace, I. K. Schuller, C. V. Segre, K. Zhang, and M. S. Kleefisch, Phys. Rev. B **36**, 3608 (1987).

[45] V. B. Grande, Hk. Müller-Buschbaum, and M. Sweitzer, Z. Anorg. Allg. Chem. **428**, 120 (1977); J. D. Jorgensen, H.-B. Schüttler, D. G. Hinks, D. W. Capone II, K. Zhang, M. B. Brodsky, and D. J. Scalapino, Phys. Rev. Lett. **58**, 1024 (1987).

[46] M. E. Lines and A. M. Glass, *Principles and Applications of Ferroelectrics and Related Materials* (Oxford University Press, Oxford, 1977).

[47] R. J. Birgeneau, C. Y. Chen, D. R. Gabbe, H. P. Jenssen, M. A. Kastner, C. J. Peters, P. J. Picone, T. Thio, T. R. Thurston, H. L. Tuller, J. D. Axe, P. Böni, and G. Shirane, Phys. Rev. Lett. **59**, 1329 (1987); P. Böni, J. D. Axe, G. Shirane, R. J. Birgeneau, D. R. Gabbe, H. P. Jenssen, M. A. Kastner, C. J. Peters, P. J. Picone, and T. R. Thurston, Phys. Rev. B **38**, 185 (1988).

[48] R. M. Fleming, B. Batlogg, R. J. Cava, and E. A. Rietman, Phys. Rev. B **35**, 7191 (1987); A. Aharony, R. J. Birgeneau, A. Coniglio, M. A. Kastner, and H. E. Stanley, Phys. Rev. Lett. **60**, 1330 (1988).

[49] E. T. Heyen, R. Liu, M. Cardona, S. Piñol, R. J. Melville, D. McK. Paul, E. Morán, and M. A. Alario-Franco, Phys.

Rev. B **43**, 2857 (1991); E. T. Heyen, G. Kliche, W. Kress, W. König, M. Cardona, E. Rampf, J. Prade, U. Schröder, A. D. Kulkarni, F. W. de Wette, S. Piñol, D. McK. Paul, E. Morán, and M. A. Alario-Franco, Solid State Commun. **74**, 1299 (1990).

[50] T. Egami, W. Dmowski, J. D. Jorgensen, D. G. Hinks, D. W. Caponne II, C. V. Segre, and K. Zhang, Rev. Solid State Sci. **1**, 247 (1987).

[51] S. Massidda, N. Hamada, Jaejun Yu, and A. J. Freeman, Physica C **157**, 571 (1989).

[52] See W. A. Harrison, *Electronic Structure and the Properties of Solids* (Dover, New York, 1989), p. 46.

[53] S. Louie, Phys. Rev. B **22**, 1933 (1980).

[54] D. Emin, in *Physics and Material Science of High Temperature Superconductors-II*, edited by R. Kossowski, N. Raveau, and S. Patapis (Klumer, Netherlands, 1992).

[55] For a review see R. Micnas, J. Ranninger, and S. Robaszkiewicz, Rev. Mod. Phys. **62**, 113 (1990).

[56] J. Zhong and H.-B. Schüttler, Phys. Rev. Lett. **69**, 1600 (1992).

[57] K. Yonemitsu, A. R. Bishop, and J. Lorenzana, Phys. Rev. Lett. **69**, 965 (1992).

[58] K. Moulopoulos and N. W. Ashcroft, Phys. Rev. Lett. **69**, 2555 (1992).

[59] E. P. Wigner, Trans. Faraday Soc. **34**, 678 (1938).

[60] P. W. Anderson, Phys. Rev. Lett. **34**, 953 (1975).

[61] S. Robaszkiewicz, R. Micnas, and J. Ranninger, Phys. Rev. B **37**, 180 (1987).

[62] Y. Bar Yam, Phys. Rev. B **39**, 6501 (1991); **43**, 359 (1991).

[63] T. Egami, Ferroelectrics **130**, 15 (1992).

[64] L. E. Reichl, *A Modern Course in Statistical Physics* (University of Texas Press, Austin, 1980).

[65] D. Emin, Phys. Rev. Lett. **62**, 1544 (1989).

[66] See, for example, J. C. Phillips, Phys. Rev. B **46**, 8542 (1992); in *Lattice Effects in High-T_c Superconductors*, edited by Y. Bar-Yam (World Scientific, Singapore, 1992), p. 3; Y. Bar Yam, *ibid.*, p. 177; J. A. Krumhansl, *ibid.*, p. 503; J. Mustre-de Leon *et al.*, *ibid.*, p. 163; K. H. Johnson, D. P. Clougherty, and M. E. McHenry, Mod. Phys. Lett. B **3**, 1367 (1989).
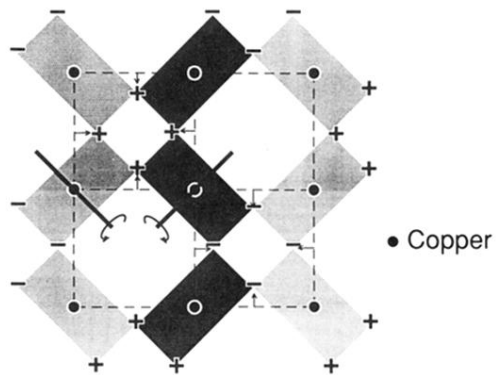
FIG. 9. Plain view of the CuO_2 plane indicating the pattern of oxygen displacements used in the 2×2 model. The shaded rectangles are the CuO_4 plaquettes; the darkness of the shading differentiates the sense of the tilt. Arrows indicate the in-plane ($\Delta O1_{xy}$) displacements and the plusses and minuses indicate the out-of-plane displacements ($\Delta O1_z$) of the O1 ion. Two of the plaquette tilt axes are shown as bars. The in-plane displacements are magnified for clarity.